

---

# Two-Dimensional Simulations of Plastic-Shell, Direct-Drive Implosions on OMEGA

## Introduction

In direct-drive inertial confinement fusion (ICF),<sup>1</sup> nominally identical beams of a laser are incident on a nearly spherically symmetric target. The target's outer surface ablates, driving the shell inward like a rocket. The shell first accelerates and then, shortly after the laser drive is turned off, coasts before decelerating toward peak compression; disassembly then follows. The goal is to implode the target, resulting in sufficiently high temperatures and densities to propagate a self-sustaining burn wave through the target, giving rise to energetic neutrons with a total energy greater than the laser energy. Ignition target designs require layers of cryogenic deuterium–tritium (DT) ice<sup>2</sup> and relatively high laser energies such as those available on the National Ignition Facility (NIF).<sup>3</sup> To provide an understanding of target dynamics, a large number of implosions on the 60-beam OMEGA laser<sup>4</sup> have been devoted to warm capsules,<sup>5–8</sup> which include plastic (CH) shells filled with deuterium (D<sub>2</sub>) gas. While a number of papers have been written on the experimental results from CH-shell implosions on OMEGA,<sup>5–8</sup> the range of nonuniformity wavelengths that influence fusion yields has been an outstanding question.

In this article, a detailed analysis of the CH-shell implosions using one- and two-dimensional simulations and analytical modeling is performed. The goal of this work is to identify, by using the hydrodynamic code *DRACO*,<sup>9</sup> the nonuniformity seeds that influence target performance. Mechanisms that influence yields are also identified. In addition, comparisons to experimental results are presented.

Imperfect illumination and target roughness seed the nonuniformity growth in direct-drive implosions. The incident laser irradiation on the target includes nonuniformities that result from energy and power imbalances between beams and from nonuniformities within each beam. While the former will be shown to result in long-wavelength ( $\ell < 10$ , where  $\ell = 2\pi R/\lambda$  is the Legendre mode number,  $R$  is the target radius, and  $\lambda$  is the nonuniformity wavelength) perturbations that lead

to an overall deformation of the shell, the latter manifest themselves in the intermediate-wavelength ( $10 < \ell < 50$ ) and short-wavelength ( $\ell > 50$ ) nonuniformities that may lead to shell breakup during the acceleration phase as well as a disruption in final fuel assembly.

Nonuniformities grow due to the Rayleigh–Taylor (RT) instability<sup>10</sup> during the acceleration phase of the implosion. The RT growth rates are smaller than classical values due to the ablative effects.<sup>10–13</sup> Nevertheless, the RT growth factors of the short-wavelength modes in the thin shells are large enough to compromise shell integrity during the acceleration phase. Shell breakup results in degradation in the shell's compressibility, which leads to a reduction in the final core temperature and density and consequently a reduction in the neutron-production rates.

Nonuniformity growth during the coasting and deceleration phases of the implosions is seeded by feedthrough to the inner surface of the shell. As will be shown later in the text, the fuel–pusher interface distortions grow significantly during the coasting phase because of convergent effects (Bell–Plesset growth).<sup>14,15</sup> Further, truncation of the neutron-production rate occurs due to the flow of fuel into the colder bubbles at the D<sub>2</sub>–CH interface during shell deceleration. Truncation is also caused by the increased heat conduction out of the core due to the larger surface area caused by shell distortions.

This article is organized as follows: (1) one-dimensional and multidimensional hydrodynamic modeling are described; (2) overall shell dynamics is discussed; (3) the four phases of the implosion (shock transit, acceleration, coasting, and deceleration) are analyzed in the context of single-mode growth; (4) multidimensional simulations of beam-to-beam imbalances and single-beam nonuniformity are described, and the combined effects of all nonuniformity sources are discussed; and (5) conclusions are presented.

### Radiation-Hydrodynamics Modeling

The one-dimensional (1-D) target dynamics discussed in this article is modeled using the code *LILAC*,<sup>16</sup> which has been described extensively in the literature and is not discussed any further.

Multidimensional behavior (2-D) of plastic targets is modeled using the code *DRACO*.<sup>9</sup> *DRACO* is a one-, two-, and three-dimensional arbitrary Lagrangian Eulerian (ALE) code based on a structured mesh. The implosions described here are simulated in one and two dimensions. The compressible hydrodynamic scheme is based on the work by Amsden *et al.*<sup>17</sup> Shocks are treated using the scheme of Wilkins.<sup>18</sup> Several artificial grid-smoothing algorithms are available to control numerical grid distortions (bowties and herringbone distortions). These are based on Refs. 17–19; only Ref. 19 is used in this work.

In a purely Lagrangian mode, interfaces between materials are maintained at cell edges; however, a significant growth of perturbations results in a severely distorted grid. As a result, the grid must be “rezoned” for the simulation to proceed. The new grid can be constructed using several prescriptions. While some grid movement options are heuristically derived, others are based on Winslow-regridding-type<sup>20</sup> schemes. *DRACO* allows for cells with mixed materials resulting from this grid rezoning. Rezoning is possible through a first-order (donor-cell) or a direction-split second-order scheme.<sup>21</sup> Material interfaces are reconstructed before every rezoning step using a scheme based on Young’s method,<sup>22</sup> which has been extended to allow for the distorted Lagrangian cells. In this scheme, the interface between materials in a cell is represented by a straight line; the slope of this line is obtained through the gradient of the fractional volumes occupied by the material in the neighboring cells.

The pressure in each mixed-material cell is obtained by adding the partial pressures of the constituent cell materials. A single temperature for the materials in the cell is obtained using the prescription described in Ref. 23. While this interface tracking scheme cannot be used to model turbulent regimes,<sup>22</sup> it has been used to model the highly nonlinear growth of buried layers that burn through to the corona.<sup>9</sup>

Various physical processes, such as heat conduction, radiation transport, etc., are treated using an operator splitting procedure. *DRACO* includes the deposition of laser energy through ray tracing and inverse bremsstrahlung. Both normal-incidence laser energy deposition and the ray-trace approach are

used in this work. Since normal incidence does not include refractive energy losses, it can significantly overestimate the energy coupled to the target. Consequently, the laser pulse shape is iteratively adjusted in 1-D simulations to provide the same overall dynamics of the implosion, including shock-breakout times, the final convergence of the shell, ablation velocities, density scale lengths, etc., as obtained with a full ray trace. This modified pulse shape is used in two-dimensional (2-D) simulations involving modes  $\geq 20$ . Spherically symmetric 2-D simulations with this modified pulse shape compare very well with 1-D simulations using a full ray trace. For simulations that include only long-wavelength modes, we use a refractive ray trace. This ray trace uses a quasi-1-D scheme, where rays are not allowed to cross angular sector boundaries. This scheme accounts for refractive losses reasonably accurately when the distortions are of relatively long wavelengths. In this technique, an angular spectrum describing the distribution of energy with angle of incidence is launched from a chosen surface each time step. This distribution takes into account both the single-beam ray distribution and beam overlap. In the limit of a spherically symmetric problem, this approach yields the same results as a full ray trace.

Several equation-of-state options (ideal gas, *SESAME*,<sup>24</sup> Thomas–Fermi,<sup>25</sup> and QEOS<sup>26</sup>) are available; the analytic Thomas–Fermi formulation is used for the simulations described in this work. Heat conduction and multigroup diffusive radiation transport are included. Tabular opacities assuming local thermal equilibrium are used for the materials while in unmixed cells. An ion-number weighted opacity is used in mixed cells for radiation transport. Radiation transport is solved in parallel across several processors.

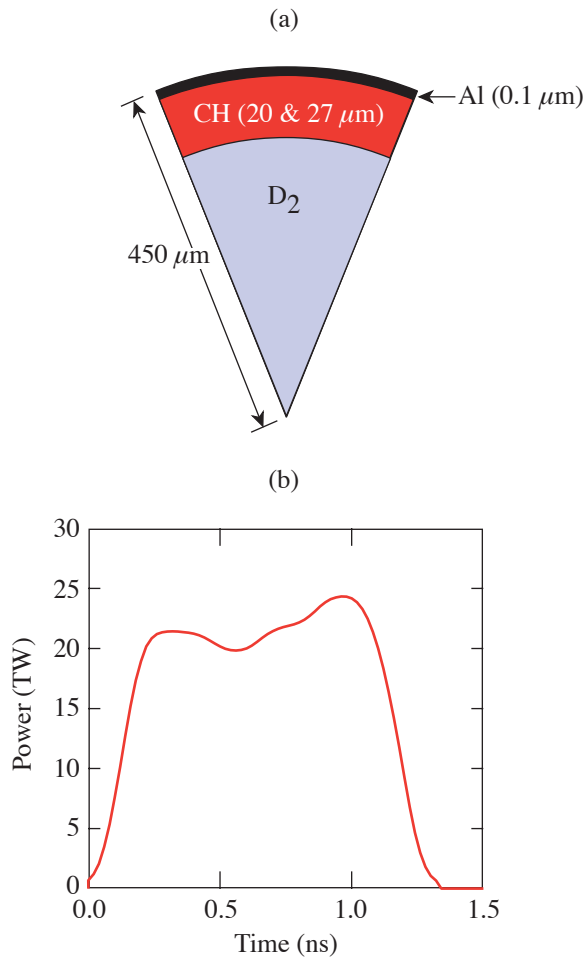
The simulations use the “group-parallel” approach where each energy group is solved on one processor and the resulting radiation energy density is broadcast to all other processors. Four radiation groups, reduced from very fine opacity tables,<sup>27</sup> are included in all the calculations in this work. The choice of the four energy groups is optimally made to closely match the 1-D dynamics corresponding to 48 energy groups. The parallel scientific library, PetSc,<sup>28</sup> is used to solve the diffusion equation via a preconditioned conjugate-gradient scheme. Message Passing Interface (MPI)<sup>29</sup> is used to communicate between processors.

Particle production from nuclear reactions is calculated using Ref. 30. Alpha-particle transport and depletion of fuel material for modeling ignition are included in *DRACO* but are not necessary in simulating OMEGA target implosions.

*DRACO* has been tested extensively against analytic problems (shock-tube problems, blast-wave problems, etc.), against other codes (*LILAC*,<sup>17</sup> *ORCHID*<sup>31</sup>), and against the ICF post-processor described in Ref. 32 for single-mode growth. Good agreement is obtained with the known solutions for all the problems considered.<sup>9</sup>

### Shell Dynamics

This work focuses on targets with plastic (CH) shells filled with  $D_2$  gas. Two cases are considered (Fig. 99.1): (1) a 20- $\mu\text{m}$ -thick CH shell with 15 atm of  $D_2$  with a convergence ratio  $CR \sim 13$  ( $CR$  is defined as the ratio of the initial radius to the



TC6574

Figure 99.1

(a) Plastic-shell targets of two thicknesses—20  $\mu\text{m}$  and 27  $\mu\text{m}$ —with  $D_2$  fills were considered in this work. (b) The pulse shape (1-ns square) used to irradiate these targets sets the shell on a relatively high adiabat ( $\sim 5$ ).

compressed radius of the fuel–shell interface at the peak of the neutron production); (2) a 27- $\mu\text{m}$ -thick CH shell with 15 atm of  $D_2$  ( $CR \sim 12$ ). A 1-ns square pulse with  $\sim 23$  kJ of energy is used to irradiate these targets with full beam smoothing [two-dimensional smoothing by spectral dispersion<sup>33</sup> (2-D SSD) with polarization smoothing (PS)<sup>34</sup>]. Case (1) has been chosen to illustrate implosion dynamics (Fig. 99.2). The laser pulse and shell acceleration history are shown in Fig. 99.2(a). The magnitude of the gradient of the natural logarithm of the pressure,  $|\partial \ln P / \partial r|$ , is shown in Fig. 99.2(b). The dark lines correspond to shock trajectories. The dashed line is the trajectory of the fuel–shell interface. Since the rise time of the laser is relatively fast ( $\sim 200$  ps), a strong shock is driven into the target, setting the shell material on a high adiabat,  $\alpha \sim 5$ , defined as the ratio of the pressure at a given density to the cold Fermi pressure at that density. The rarefaction wave launched at the breakout of the shock (at  $\sim 0.4$  ns) from the shell reaches the ablation surface, where a compression wave is consequently launched into the target. At this time the shell starts to accelerate inward as indicated by the negative acceleration in Fig. 99.2(a). The compression wave travels down the decreasing density gradient and breaks out of the shell as a shock (at  $\sim 0.8$  ns). Both shocks meet in the gas (at  $\sim 1$  ns) before reaching the center. The four main phases of the implosion are shown in Fig. 99.2(a). The acceleration phase occurs after shock transit and continues until shortly after the laser pulse turns off (at  $\sim 1.4$  ns), at which time the shell starts traveling with a constant velocity (coasting phase). Deceleration of the shell begins when the shock reflects from the center and returns to the shell (at  $\sim 1.75$  ns). This impulsive deceleration is followed by a period of continuous deceleration due to pressure buildup in the gas [Fig. 99.2(a)].

Shock breakout is later in the thicker, 27- $\mu\text{m}$  implosion (at  $\sim 0.5$  ns compared to  $\sim 0.4$  ns). The more-massive, 27- $\mu\text{m}$ -thick shell moves more slowly during the coasting phase than the 20- $\mu\text{m}$ -thick CH shell. It therefore coasts for a longer time ( $\sim 650$  ps compared to  $\sim 350$  ps). The shell’s convergence ratio for the coasting phase, defined as the ratio of the shell radius at the beginning and end of the coasting phase, is 3.0 for the thicker shell compared to 2.2 for the thinner shell.

### Single-Mode Simulations

In this section, the evolution of nonuniformities through single-mode simulations is described. The seeding of nonuniformities is described in “Shock Transit.” The growth during the three phases—acceleration, coasting, and deceleration—is described in subsequent subsections.

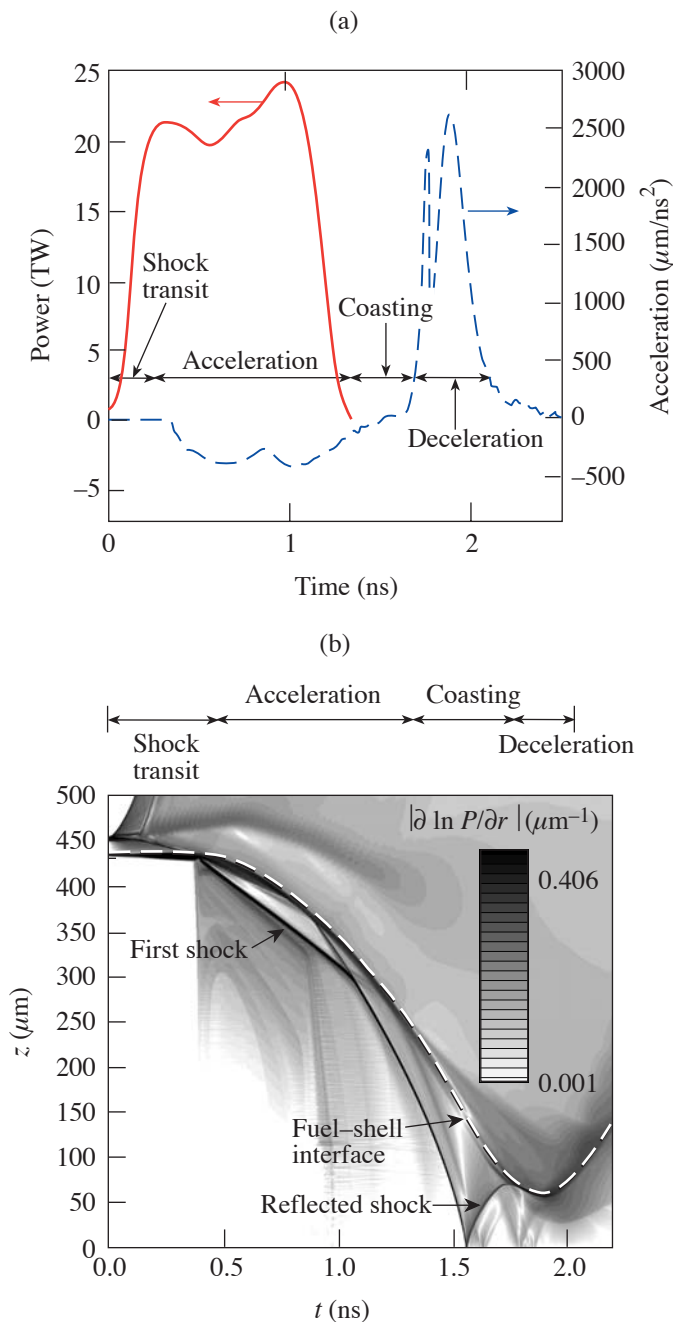


Figure 99.2  
 (a) Acceleration and laser pulse shape history (1-ns square) for the 20- $\mu\text{m}$  CH shell irradiated with a 1-ns square pulse at 23 kJ of energy. (b) Contour plot of the magnitude of the gradient of the natural log of pressure for the target in (a). The darker contours correspond to shock trajectories. The dashed line is the trajectory of the fuel-shell interface. Also shown is the duration of the four phases of the implosion (shock-transit, acceleration, coasting, and deceleration).

### 1. Shock Transit

As mentioned in the last section, a strong shock is launched into the shell at the beginning of the pulse. Since there is no significant acceleration of the ablation front during the shock propagation through the shell, the shell nonuniformities are not susceptible to Rayleigh–Taylor instability. The perturbations, however, grow during this phase because of nonuniform laser illumination (power imbalance, beam mistiming, and single-beam nonuniformities or laser imprint). The initial outer-surface roughness, in general, can be amplified as well by Richtmyer–Meshkov<sup>35</sup> instability at the ablation front; such a growth, however, is totally stabilized by ablation.<sup>36</sup> As a result, the mode spectrum due to the initial outer-surface roughness does not significantly change during shock transit.

First, the evolution of long-wavelength modes seeded by power imbalance among the 60 OMEGA beams is described. This imbalance is due to beam mispointing, different beam shapes, beam mistiming, and energy imbalance between beams. The resultant laser illumination amplitudes due to all these sources are shown in Fig. 99.3 for the dominant modes. The tilt that might be introduced to each beam pulse shape is not included in these calculations. Azimuthal asymmetries in each phase plate are also not modeled. The perturbation amplitude for a given mode is obtained by overlapping and decomposing

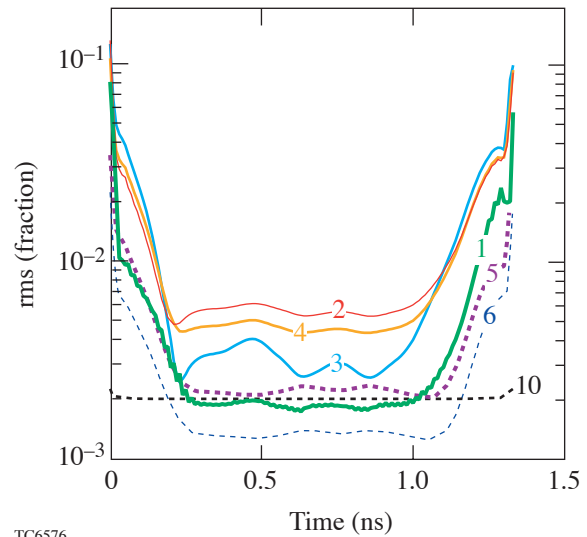


Figure 99.3  
 Modal amplitudes of the dominant modes due to beam imbalances as a function of time. The early-time large amplitudes correspond to beam mistiming. The values at the peak of the pulse (0.2 ns to 1.1 ns) are due to energy imbalance between beams, beam mispointing, and differences in spot shapes.

the 60-beam energies on a sphere into spherical harmonics. The amplitude of the corresponding Legendre mode is obtained by adding all the  $m$ -mode amplitudes in quadrature. The phase of the mode is chosen to be that of the  $m = 0$  spherical harmonic. The large perturbation amplitudes of the Legendre modes correspond to the beginning of the laser pulse and are mainly due to beam mistiming ( $\sim 12$ -ps rms). Once the peak intensity is reached, the nonuniformity reaches its asymptotic value corresponding to the energy imbalance in the beams (beam energies of the 60 OMEGA beams from a typical shot are used to apply energy imbalance), beam mispointing ( $\sim 24$ - $\mu\text{m}$  rms),<sup>37</sup> and differences in beam shapes ( $\sim 11$ - $\mu\text{m}$  rms in super-Gaussian radius and  $\sim 0.6\%$  rms in super-Gaussian exponent). These values are typical of OMEGA. The target is assumed to be at the target chamber center. (Typically on OMEGA, plastic shells are within  $5 \mu\text{m}$  of target chamber center at shot time.) Mode numbers 2 and 4 have the largest amplitudes as indicated by Fig. 99.3. Mode number 10 is due to the 60-beam OMEGA geometry.

A model that describes the seeding of the ablation surface due to the long-wavelength nonuniformities is described in Appendix A. This sharp-boundary model relates the modal amplitudes at the fuel-shell interface to the modulation in drive pressure, which in turn is related to the modulations in laser intensity using the “cloudy-day” model.<sup>38</sup> Here, the results of this model are compared with the full 2-D simulation involving modes up to 10. The modal amplitudes of the  $D_2$ -CH interface at the onset of the acceleration phase are shown in Fig. 99.4 for the  $20$ - $\mu\text{m}$ -thick implosion. These are obtained by decomposing the interface perturbations from the 2-D simulation into Legendre modes (solid circles). The amplitudes obtained from the model (x’s) are also shown in Fig. 99.4. The results of the simulation are reproduced well by the simple model.

Next, the evolution of target nonuniformities caused by single-beam modulations (laser imprint) is described. Since laser imprint stays in the linear regime during shock transit, the mode spectrum is calculated by carrying out a series of single-mode, 2-D simulations up to the beginning of the acceleration phase. Imprint simulations are performed by imposing a 1% single-mode modulation in the laser illumination. 1-THz, 2-D SSD<sup>32</sup> is applied to the perturbation amplitudes. SSD is modeled nondeterministically. Each mode is characterized by a coherence time given by  $t_c = [\Delta\nu \sin(n_c \pi \ell / \ell_{\max})]^{-1}$ , where  $\ell_{\max} = 2\pi R_0 / \delta$  is the mode number corresponding to half the speckle size  $\delta$  ( $\delta = 2.35 \mu\text{m}$  for the OMEGA system),  $R_0$  is the initial outer shell radius,  $\Delta\nu$  is the SSD bandwidth, and  $n_c$  is

the number of color cycles on the laser system. The phase of the mode is chosen randomly every coherence time (the “flipping” approximation). This scheme mimics the average response of the target to the laser modulations. Averaged over time  $T$ , the single-beam rms nonuniformity, for a constant-intensity laser pulse, decreases as  $\sqrt{t_c/T}$ . For each mode in the simulation, the sequence of phases corresponds to a discrete two-state random walk. The number of the statistically independent phase sequences is limited by a finite maximum angular spread  $\Delta\theta$  of the light propagating through the laser. The averaged mode amplitude cannot be reduced by SSD to levels below the asymptotic limit. This limit is inversely proportional to the square root of the number of statistically independent speckle patterns  $N_{\text{stat}}(\lambda) = (4S_{\text{max}}^x/\lambda)(4S_{\text{max}}^y/\lambda)$ , where  $\lambda = 2\pi R_0/\ell$  is the nonuniformity wavelength,  $S_{\text{max}}^{x(y)} = F\Delta\theta^{x(y)}$  is the maximum spatial shift in the  $x(y)$  direction,  $F = 180 \text{ cm}$  is the focal length, and  $\Delta\theta^x = 50 \mu\text{rad}$  and  $\Delta\theta^y = 100 \mu\text{rad}$  for the OMEGA laser system. The asymptotic limits are modeled in the flipping approximation by selecting only  $N_{\text{stat}}$  independent choices for the sign of the nonuniformity amplitude. The average over a large number of runs will then correspond to the expected response of the target to the single mode. The calcu-

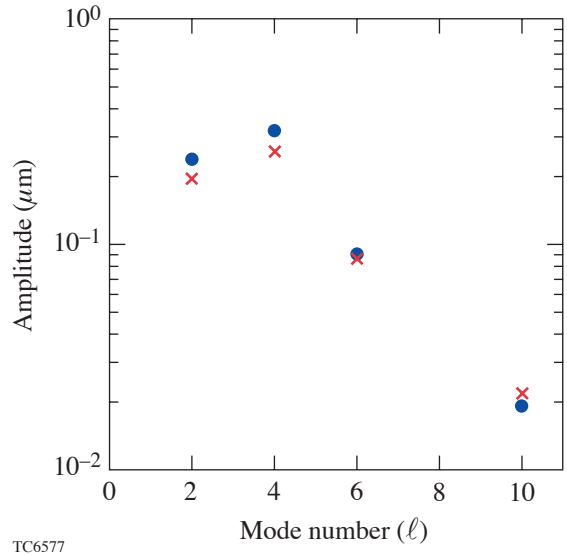


Figure 99.4 Single-mode amplitudes of the fuel-shell interface at the beginning of acceleration from a 2-D simulation for the  $20$ - $\mu\text{m}$ -thick CH implosion (solid circles). The values obtained from the model described in Appendix A are also shown (x’s). The “cloudy-day” model relates the amplitudes at the fuel-shell interface to modulation in laser drive. Good agreement between the simulations and model indicates that the seeding of the interface is well understood.

lated ablation-front amplitude at the beginning of the acceleration phase  $\eta_{\%}$  is a decaying function of the mode number  $\ell$ .<sup>39</sup> This is due to both the shorter decoupling time and the stronger dynamic overpressure stabilization of the higher- $\ell$  modes. When the effect of SSD is included, the imprint efficiency scales linearly with the mode wavelength. For the plastic shells driven by a 1-ns square pulse with 1-THz, 2-D SSD, the numerical calculations give the following ablation-front amplitude per 1% laser nonuniformity:

$$\eta_{\%} \approx 6 \times 10^{-5} (6.7 + 2\pi R_0 / \ell), \quad (1)$$

where the initial shell radius  $R_0$  and  $\eta_{\%}$  are in microns. To calculate the mode spectrum at the ablation front due to the laser imprint, amplitude  $\eta_{\%}$  is multiplied by  $\sigma_{\text{rms}}$  of the laser nonuniformity of a particular mode.

Calculation of the laser  $\sigma_{\text{rms}}(\ell)$  includes the effects of the distributed phase plates (DPP's).<sup>40–42</sup> Laser beams are phase converted by being passed through the DPP's on the OMEGA laser. The DPP's improve the focused single-beam uniformity by removing the large-scale beam structure with a higher imprint efficiency [see Eq. (1)], leaving intensity profiles with a well-controlled envelope modulated by fine-scale speckle with a lower imprint efficiency. An analytical model that describes this fine speckle<sup>43</sup> is used to model the static single-beam nonuniformity in 2-D simulations in which the  $\ell$ -mode nonuniformity is given as

$$\sigma_{\text{rms}}^2(\ell) = \frac{16\ell}{\pi \ell_{\text{max}}^2} \left[ \cos^{-1} \left( \frac{\ell}{\ell_{\text{max}}} \right) - \frac{\ell}{\ell_{\text{max}}} \sqrt{1 - \left( \frac{\ell}{\ell_{\text{max}}} \right)^2} \right]. \quad (2)$$

This mode spectrum was confirmed experimentally in Ref. 44. The illumination nonuniformity given by Eq. (2) is shown in Fig. 99.5 as a function of mode number. Note that the laser nonuniformity amplitudes increase initially as a function of mode number (up to  $\ell \sim 600$ ), opposite to the decay in the imprint efficiency with the wave number [Eq. (1)].

Polarization smoothing further reduces the amplitude by a factor of  $\sqrt{2}$ .<sup>34</sup> Further reduction in modal amplitudes is obtained with beam overlap. This reduction factor is obtained by comparing the result of overlapping 60 OMEGA beams on a sphere with the single-beam DPP amplitudes. A reduction factor of  $\sqrt{12}$  reproduces the resultant overlapped amplitude pattern on a sphere. Overall amplitudes in the DRACO simulation are correspondingly reduced. The resulting imprint

spectrum (dotted line) at the ablation front is plotted in Fig. 99.6. Figure 99.6 also shows the ablation-surface amplitude due to imprint from one multimode DRACO simulation up to mode number 200 (solid line). The multimode simulation

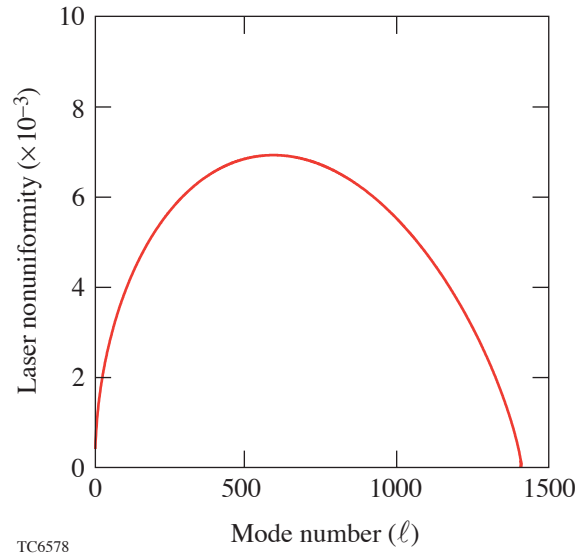


Figure 99.5

Nonuniformity spectrum due to phase-plate speckle. This nonuniformity peaks around  $\ell \sim 600$ .

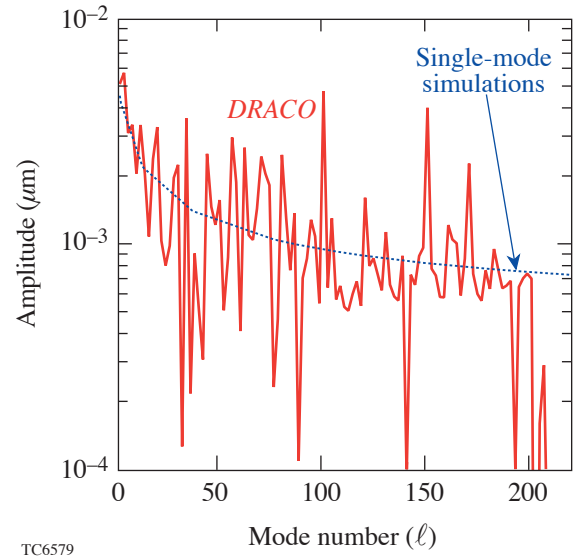


Figure 99.6

Imprint spectrum from single-mode simulations (dotted line) and multimode simulation (solid line). The good agreement confirms linear behavior of imprint. Note that imprint efficiency decreases with increasing mode number. This is opposite in behavior to the laser nonuniformity (Fig. 99.5).

shows variations in the imprint spectrum due to the nondeterministic scheme used to model SSD. Good agreement, on average, between the two calculations confirms the linear behavior of imprint prior to shell acceleration.

The seeding due to all three nonuniformity sources is compared in Figs. 99.6 and 99.7. The contribution of the ablation-surface nonuniformity from power imbalance and surface roughness<sup>45</sup> is shown in Fig. 99.7. The comparison of this spectrum with Fig. 99.6 shows that the main contribution to the low- $\ell$  modes comes from beam imbalances. Surface roughness has a smaller contribution at low  $\ell$ . Laser imprint dominates the intermediate ( $10 < \ell < 50$ )- and high- $\ell$ -mode seeding (not shown).

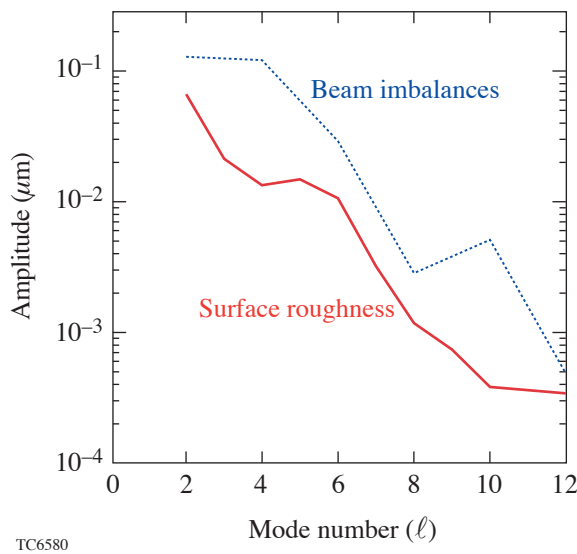


Figure 99.7  
Long-wavelength perturbations at the ablation surface due to beam imbalances (dotted line) and surface roughness (solid line) at the start of acceleration. Beam imbalances provide the larger contribution to long-wavelength nonuniformity seeds.

## 2. Acceleration Phase

The two main sources of perturbation growth during the acceleration phase are (1) the RT instability caused by the opposite directions of the pressure and density gradients at the ablation front and (2) the secular growth due to the asymmetries in the laser drive. The latter growth is important only for low- $\ell$  modes where the wavelength is much longer than the distance between the laser deposition region and the ablation front (conduction zone). Shorter-wavelength drive nonuniformities are smoothed out by the thermal conduction in the conduction zone (the cloudy-day effect). In addition, the RT

growth rate increases with mode number; therefore, secular growth becomes negligible at the shorter wavelengths.

The relative importance of the secular growth versus the RT growth for different long-wavelength modes is illustrated in Appendix B using a simple model. The model indicates that the final amplitudes at the end of the acceleration phase caused by secular growth alone are significantly smaller than when RT growth is also included. This suggests that power balance is extremely important during the period of shock transit when the seeds for RT growth are established. During acceleration, beam imbalances are less important because the resulting secular growth is dominated by RT growth. This is confirmed by the results of the simulations shown in Fig. 99.8. In simulation 1 (solid line), beam imbalance is turned off at the start of acceleration, whereas in simulation 2 (dotted line), it is retained throughout the laser pulse. The ablation-surface amplitudes vary by less than 20%, confirming that beam balance is important primarily during shock transit.

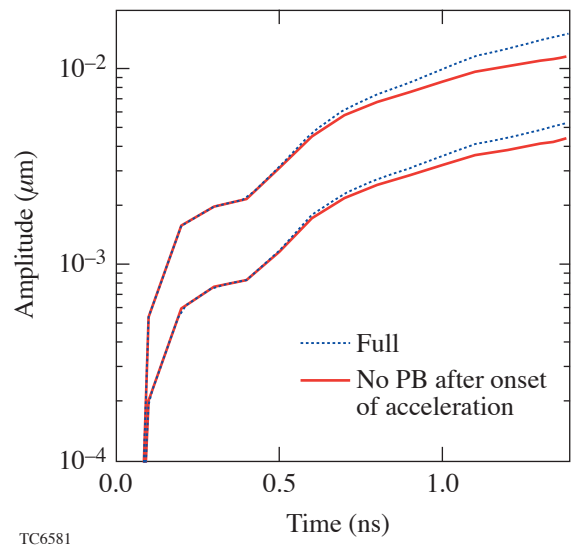


Figure 99.8  
Amplitudes of the  $D_2$ -CH interface versus time for mode numbers 2 and 4 for beam imbalances throughout the pulse (dotted) and beam imbalances imposed on target only until the start of acceleration (solid). The small effect of beam imbalances during the acceleration phase indicates that long-wavelength modes are seeded primarily during shock transit.

Next, evolution of the intermediate ( $10 < \ell < 50$ )- and short-wavelength modes ( $\ell > 50$ ) is considered. The main seed of these modes comes from the single-beam nonuniformity (laser imprint). The initial spectrum of imprint perturbations at the ablation surface is peaked at the low- $\ell$  modes (Fig. 99.6). The RT growth rate, however, increases with the mode number,

shifting the spectrum maximum during acceleration toward shorter wavelengths. It is well known that mass ablation significantly reduces RT growth rate compared to the classical limit.<sup>11–13</sup> As shown in Ref. 44, a rather complicated expression for the growth rate can be fitted with much simpler formulas:

$$\gamma = \alpha_1 \sqrt{kg} - \beta_1 k V_a, \quad Fr \gg 1, \quad (3)$$

$$\gamma = \alpha_2 \sqrt{\frac{kg}{1+kL_m}} - \beta_2 k V_a, \quad Fr \ll 1, \quad (4)$$

where  $Fr = V_a^2 / (gL_0)$  is the Froude number,  $L_0$  is the characteristic thickness of the ablation front,  $L_m$  is the minimum density-gradient scale length, and  $V_a$  is the ablation velocity defined as the mass ablation rate divided by the shell density. The coefficients  $\alpha_{1,2}$  and  $\beta_{1,2}$  are functions of the Froude number and the effective power index for thermal conduction  $\nu$ . The dispersion formulas described in Eqs. (3) and (4) have been verified experimentally in Ref. 45 for CH. For the 20- $\mu\text{m}$ -thick plastic shell considered in this article, the time-averaged acceleration, ablation velocity, ablation-front thickness, and power index, respectively, are  $g = 320 \mu\text{m}/\text{ns}^2$ ,  $V_a = 3.2 \mu\text{m}/\text{ns}$ ,  $L_0 = 0.18 \mu\text{m}$ ,  $L_m = 0.72 \mu\text{m}$ , and  $\nu = 1$ ; therefore, the Froude number is small,  $Fr = 0.18$ , and Eq. (4) can be used to calculate the RT growth rate. The fitting procedure described in Ref. 44 gives the following coefficients:  $\alpha_2 = 0.94$  and  $\beta_2 = 1.50$ . Growth rates from single-mode simulations (solid circles in Fig. 99.9) compare very well with this analytic formula (dotted line in Fig. 99.9). Each simulation point in Fig. 99.9 is a single-mode simulation with a small amplitude perturbation to the laser nonuniformity, such that the mode growth remains in the linear regime during the acceleration. Equation (4) also indicates that the cutoff occurs at very high  $\ell$  modes,  $\ell_c = 1220$ , and the growth rate does not decrease significantly even for mode numbers as high as  $\ell \sim 600$  for these plastic ablaters. Modes above  $\ell \sim 600$ , however, have a much smaller initial amplitude and experience nonlinear saturation. Their contribution to the total nonuniformity budget, therefore, is insignificant.

It is instructive to point out the stabilizing role of the radiation. Reabsorption of the emission from the corona by the shell raises the shell adiabat near the ablation front, leading to adiabat shaping by radiation in the shell. This increases the ablation velocity (from  $\sim 2.2 \mu\text{m}/\text{ns}$  to  $\sim 3.2 \mu\text{m}/\text{ns}$ ) and the density-gradient scale length (from  $L_m = 0.1 \mu\text{m}$  to  $0.7 \mu\text{m}$ ). Since the density is much sharper when the radiation transport

is turned off, the Froude number increases,  $Fr = 0.7$  (compare to  $Fr = 0.18$  with radiation). Fitting the growth rate gives the following result:  $\gamma_{\text{NoRad}} = 0.92 \sqrt{kg / (1+kL_m)} - 1.59 k V_a$ . The cutoff mode number in this case increases from  $\ell_c = 1200$  to  $\ell_c = 4000$ , and the growth rate of mode  $\ell = 200$  increases from  $\gamma = 7.8 \text{ ns}^{-1}$  to  $10.1 \text{ ns}^{-1}$ . The growth rates for the cases with and without radiation transport are summarized in Fig. 99.9.

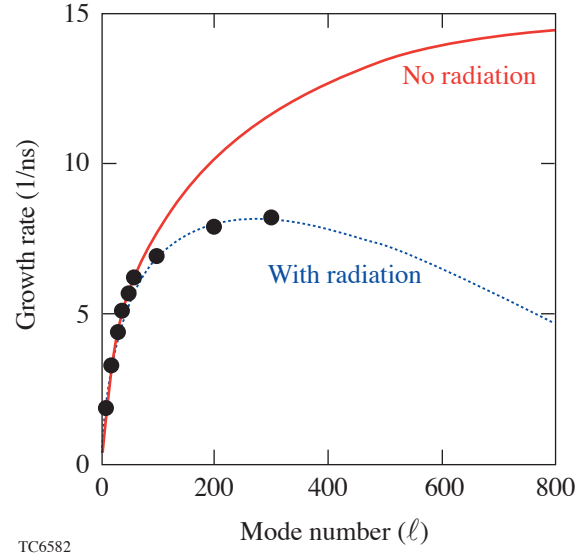


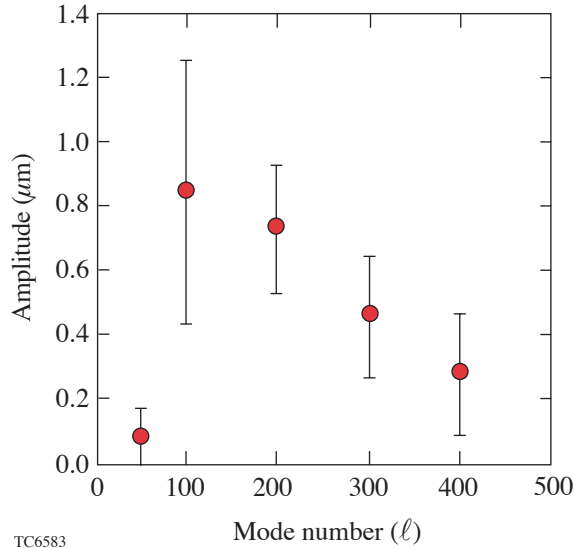
Figure 99.9

Good agreement is obtained with simulated single-mode growth rates (solid circles) and the Betti formula for plastic (dotted line). Also shown is the Betti formula for growth rates when radiation transport is not included in the simulation (solid line). Reabsorption of radiation from the corona plays an important role in stabilizing the growth of perturbations at the ablation surface.

The results from single-mode simulations using the realistic imprint amplitudes caused by the use of phase plates are shown in Fig. 99.10. SSD and polarization smoothing are applied to smooth the nonuniformity over time. Since beam smoothing is modeled nondeterministically, the average of several simulations is used for the ablation-surface amplitude. Each simulation point in Fig. 99.10 is the ablation-surface amplitude obtained from the average of five simulations with the error bar representing the standard deviation of these five simulations. It can be seen that modes up to at least 400 contribute to the ablation-surface nonuniformity. A full 2-D simulation would require, therefore, at least 400 modes to realistically model shell stability during the acceleration phase.

The more-massive, 27- $\mu\text{m}$ -thick plastic shell accelerates less ( $g = 240 \mu\text{m}/\text{ns}^2$ ) and consequently has lower growth

rates. The nonuniformity seeds at the end of the acceleration phase from feedthrough are, therefore, also smaller at the D<sub>2</sub>–CH interface.



TC6583

Figure 99.10

Single-mode amplitudes at the end of the acceleration phase. The solid circles are averages of five simulations, each with a different choice of random number seed for the nondeterministic SSD model. The error bars represent the standard deviation of the amplitude across the five simulations. The relatively large values of  $\ell = 400$  indicate that such short wavelengths will contribute significantly to the ablation-surface nonuniformity.

### 3. Coasting Phase

Shortly after the laser drive is turned off, the shell stops accelerating and starts to coast with a spatially averaged velocity that is constant in time. The coasting phase lasts until the main shock reflects from the center and begins to interact with the incoming shell. Even though the shell perturbations are not subject to the RT instability while the shell coasts inward, the perturbations are still amplified by Bell–Plesset growth. This growth is due to convergence and scales approximately as  $\eta \sim (\rho r^2)^{-1}$ . Since the shell coasts inward, the shell radius decreases and the perturbation amplitude grows. Furthermore, both the front and back surfaces of the shell and the D<sub>2</sub>–CH interface expand (in the frame of reference moving with the shell) with the local sound speed, leading to a decrease in the density that further amplifies the perturbations. In general, the equation governing the perturbation evolution in the absence of acceleration has a weak mode-number dependence.<sup>32</sup> Simulations, however, show a strong  $\ell$ -dependence of the Bell–Plesset growth, especially for long- and intermediate-wavelength modes (see Fig. 99.11). Such dependence is

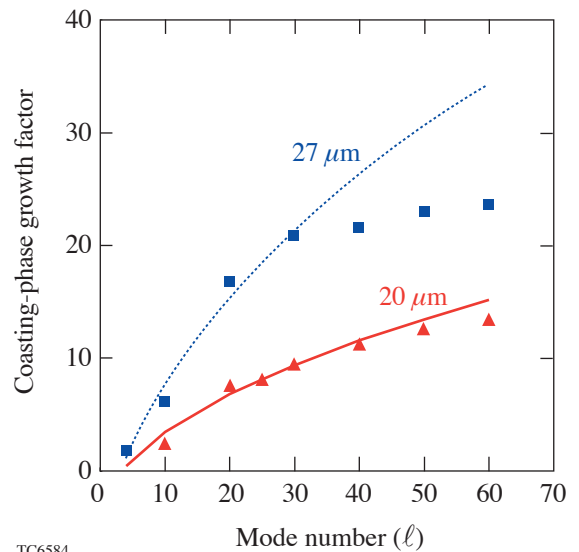
due to the differences in long- and short-wavelength growth prior to the coasting phase. Since the low- $\ell$  RT growth rate scales as a square root of the mode number  $\ell$ , the longer-wavelength perturbations have lower RT growth rates during shell acceleration. Therefore, at the end of the pulse, the velocity perturbation at the D<sub>2</sub>–CH interface is proportional to the square root of the mode number. To illustrate how mode dependence appears in the convergence growth, we adopt the simplest model for the perturbation evolution during the coasting phase:<sup>15</sup>

$$\frac{d}{dt} \left[ \frac{d(\rho r^2 \eta)}{dt} \frac{1}{\rho r} \right] = 0. \quad (5)$$

Integrating Eq. (5) twice with the initial conditions  $\eta(t = 0) = \eta_0$  and  $d\eta/dt(t = 0) = \eta'_0 \approx \sqrt{\ell/R_0 g} \eta_0$  gives the perturbation growth factor

$$\frac{\eta}{\eta_0} = C_c^2 \left[ \frac{\rho_0}{\rho} + \left( -\frac{2V_{\text{imp}}}{\rho R_0^2} + \sqrt{\frac{\ell g}{R_0}} \frac{1}{\rho R_0} \right) \int_0^t \rho(t') r(t') dt' \right], \quad (6)$$

where  $C_c$  is the shell convergence ratio during the coasting phase,  $R_0$  is the shell radius at the end of the acceleration phase,  $\rho_0$  is the density at the end of the acceleration phase, and  $V_{\text{imp}}$  is the implosion velocity. Equation (6) shows that the longer-



TC6584

Figure 99.11

Single-mode growth factors for the coasting phase for the 20- $\mu\text{m}$ -thick (triangles) and 27- $\mu\text{m}$ -thick (squares) CH implosions. The lines are  $\sim \sqrt{\ell}$  - fit to the growth factors for  $\ell < 30$ . Growth factors clearly saturate for  $\ell > 30$  for the 27- $\mu\text{m}$ -thick CH shell.

wavelength modes experience smaller growth factors, in agreement with the results of simulations (see Fig. 99.11). The behavior of shorter wavelengths ( $\ell > 50$ ), however, is different from Eq. (6). The perturbations at the  $D_2$ -CH interface for such modes decouple from the unstable ablation front during shell acceleration when  $\Delta_{\text{int}}\ell/r$  becomes greater than unity, where  $\Delta_{\text{int}}$  is the distance between the ablation front and the interface. After decoupling, the interface ripple starts to oscillate with increasing amplitude due to the convergence effects. The growth factor for such modes is defined as the ratio of the interface amplitude at the end of shell coasting to the amplitude maximum during the acceleration phase; then,  $\eta_0 \neq \sqrt{\ell/rg}\eta_0$  and  $\ell$ -dependence of the solution of Eq. (5) becomes much weaker than  $\sqrt{\ell}$ . This is confirmed in Fig. 99.11, which shows a clear saturation of the growth factors after  $\ell \sim 30$  for the 27- $\mu\text{m}$ -thick implosion. The lines in Fig. 99.11 are a  $\sqrt{\ell}$  fit to the growth factor for  $\ell < 30$ . For the 20- $\mu\text{m}$ -thick implosion, this saturation is less apparent. The 27- $\mu\text{m}$  shell moves slower during the acceleration phase; hence, it coasts for a longer time ( $C_c = 2.2$  for 20- $\mu\text{m}$  shell and  $C_c = 3.0$  for 27- $\mu\text{m}$  shell). This leads to larger coasting-phase growth factors in thicker shells. It is important to note that the larger  $D_2$ -CH growth factors during coasting partially compensate for the smaller nonuniformity seeds at the start of the coasting phase for the thicker, 27- $\mu\text{m}$  implosion. At shell stagnation, therefore, the interface distortions exhibit very little sensitivity to shell thickness.

#### 4. Deceleration Phase

The coasting phase is followed by shell deceleration when the main shock reflected from the center begins to propagate outward inside the shell. The shell at the deceleration phase is defined as the high-density portion of the CH material (according to a standard definition, the shell is bounded by the  $\rho_{\text{max}}/e$  points on both sides from the position of the maximum density  $\rho_{\text{max}}$ ; also Fig. 99.12). The fuel, together with the inner lower-density, high-temperature CH, forms the hot spot. As the shell converges and temperature inside the hot spot increases, the heat front advances outward and ablates the colder portion of the shell. Therefore, the mass of the higher-temperature hot spot increases during the deceleration phase. This is similar to the hot-spot formation in cryogenic ignition designs.<sup>46</sup> The main difference between cryogenic implosions and the gas-filled plastic implosions is that the hot spot in a cryogenic target consists only of the fuel, while the plastic implosions have two materials—fuel and CH. Since there is a mismatch in the average ion charge  $Z$  of the two materials, the density and thermal conductivity are discontinuous across the material interface. The density jump is easily obtained from the pressure continuity condition across the interface in the absence of

radiative effects. The total pressure of the ionized gas is  $p = \rho T/A$ , where  $T$  is the temperature,  $A = m_i/(1+Z)$ , and  $m_i$  is the average ion mass. Since the heat flux is continuous across the interface, the temperature must be continuous as well; therefore, the jump in density becomes

$$\frac{\rho_{\text{CH}}}{\rho_{\text{DD}}} = \frac{m_{\text{CH}}}{m_{\text{DD}}} \frac{1+Z_{\text{DD}}}{1+Z_{\text{CH}}}. \quad (7)$$

Substituting  $m_{\text{CH}} = 6.5 m_p$ ,  $m_{\text{DD}} = 2m_p$ ,  $Z_{\text{CH}} = 3.5$ , and  $Z_{\text{DD}} = 1$  into Eq. (7) gives  $\rho_{\text{CH}}/\rho_{\text{DD}} = 1.44$ , which leads to the Atwood number  $A_T = 0.18$ . Here,  $m_p$  is the proton mass. Such a density jump across the material interface creates conditions for the RT growth. There are two RT unstable regions during the deceleration phase: (1) the classically unstable CH- $D_2$  interface with  $A_T = 0.18$  and (2) the rear surface of the shell. Density profiles at peak neutron production are shown in Fig. 99.12 to illustrate this point. The simulation without radiative effects (solid) shows two distinct regions of instability: the fuel-shell interface with an Atwood number of 0.18 and a less-steep density gradient leading up to the peak density. While the first region is unstable for all mode numbers, the growth rate at the second region is significantly reduced by the density-gradient scale length and mass ablation. With radiative effects included in the calculation (dotted), however, the effective Atwood number at the interface significantly increases to

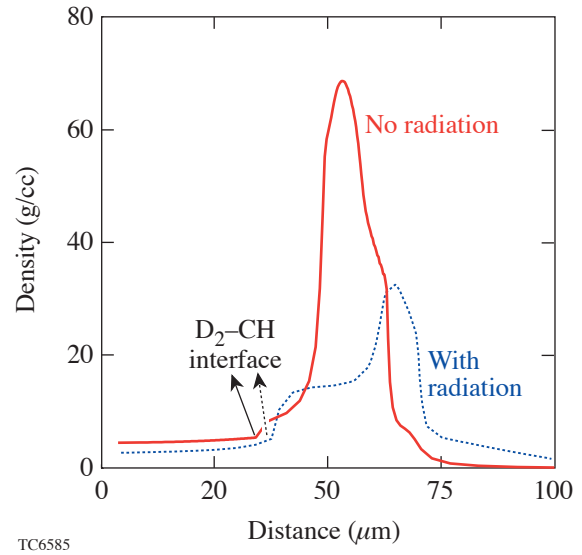


Figure 99.12

Density profiles at peak neutron production from a 1-D simulation with (dotted) and without (solid) radiation transport. Radiation plays an important role during deceleration by raising the effective Atwood number for long and intermediate wavelengths.

$\sim 0.5$  from the relatively small value of 0.18. This effect is due to the ablation of the colder shell material. As the shell material ablates and is heated by the thermal conduction from the core, the bremsstrahlung radiation increases. The radiation losses lead to additional cooling and compression of the blowoff CH. The simulation with radiation transport in Fig. 99.12 (dotted line), at peak neutron production, has a larger  $A_T$  compared to the simulation without radiation (solid line). As a consequence of this increased Atwood number, there is an increase in the RT instability growth rate for long and intermediate wavelengths. The RT instability creates a lateral flow of the fuel along the interface that moves the fuel from the hotter spike region into the colder bubbles. This leads to an effective cooling of the fuel and degradation in the neutron production rate. Such a mechanism of the neutron-yield truncation is dominant for the thicker shell, which is stable enough during the acceleration phase to maintain its integrity.

As mentioned earlier, the main shock reflected from the target center starts to propagate across the shell at the beginning of the deceleration phase. The material behind the shock stagnates, transferring the shell's kinetic energy into the internal energy of the hot spot. It is easy to understand intuitively that the larger momentum flux of the shell material across the shock results in higher hot-spot stagnation pressure. To estimate the dependence of the final hot-spot pressure  $P_f$  on the shell's parameters, we use the continuity conditions across the shock propagating inside the shell, which moves with implosion velocity  $V_{\text{imp}}$  and has density  $\rho_{\text{sh}}$ . In the shock-front frame of reference, the mass-flow continuity reads as

$$\rho_c U_2 = \rho_{\text{sh}} U_1, \quad (8)$$

where  $U_1$  and  $U_2$  are the fluid velocities ahead and behind the shock and  $\rho_c$  is the compressed density behind the shock. Since the material behind the shock stagnates in the laboratory frame of reference,  $U_2 = U_s$  and  $U_1 = V_{\text{imp}} + U_s$ , where

$$U_s \approx \sqrt{\frac{\gamma+1}{2} \frac{P_f}{\rho_{\text{sh}}}} \quad (9)$$

is the shock velocity in the strong-shock limit and  $\gamma = 5/3$  is the ratio of specific heats. Combining Eqs. (8) and (9) and using  $\rho_c \approx 4\rho_{\text{sh}}$  gives

$$P_f \sim \rho_{\text{sh}} V_{\text{imp}}^2 \sim \frac{E_{\text{kin}}}{R_{\text{hs}}^2 \Delta_{\text{sh}}}. \quad (10)$$

At shell stagnation, the kinetic energy of the shell  $E_{\text{kin}} = M_{\text{sh}} V_{\text{imp}}^2 / 2$  is transferred into the internal energy of the hot spot  $2/3 P_f R_{\text{hs}}^3$ . Equation (10) shows that the stagnation radius is proportional to the shell thickness  $R_{\text{hs}} \sim \Delta_{\text{sh}}$ ; therefore, the final pressure of the compressed fuel is larger for a "compact" shell with higher density and smaller shell thickness for a given shell kinetic energy. In other words, the kinetic energy of the converging shell heats the hot spot more efficiently in shells with larger compressibility (smaller entropy). Comparing 20- and 27- $\mu\text{m}$  shells, we conclude that the stagnation radius of the thicker shell is larger; thus the final pressure and the neutron-production rate are smaller. On the other hand, if one compares the shell that remains integral during the acceleration phase with a shell whose stability is severely compromised by RT growth, the integral shell has a lower entropy and smaller shell thickness. It, therefore, stagnates at a smaller radius reaching a higher hot-spot pressure and temperature. This leads to a larger neutron-production rate in the integral shell in comparison with the significantly distorted shell.

The larger shell thickness in the implosion with compromised shell integrity also implies that the rate at which neutron production decreases should be less steep during shell disassembly. Between the time of peak neutron production and peak compression, the neutron rate decreases due to the falling temperature in the gas. The subsequent decrease in the neutron-production rate occurs due to shell disassembly. If the shell is thicker, disassembly occurs later in the implosion as follows: The time between the interaction of the reflected shock (which is very similar for both integral and severely distorted shells) and when the shock breaks out of the shell is given by  $t_s = \Delta_{\text{sh}} / U_s$ . From Eqs. (9) and (10),  $U_s = \sqrt{E_{\text{kin}} / R_{\text{hs}}^2 \Delta_{\text{sh}} \rho_{\text{sh}}}$ . Since  $E_{\text{kin}}$  is very similar between the integral shell and severely distorted shell implosion (only a small portion of the total energy goes into lateral flow in the distorted shell implosion) and mass ( $\propto R_{\text{hs}}^2 \Delta_{\text{sh}} \rho_{\text{sh}}$ ) is conserved, the shock velocity is very similar in both cases; therefore,  $t_s \propto \Delta_{\text{sh}}$  and is longer for the thicker shell, and disassembly is delayed. Consequently, neutron production falls less steeply in the implosion where shell stability is compromised than in the implosion with an integral shell.

## Multimode Simulations

### 1. Effects of Beam-to-Beam Imbalances

We now turn to multimode simulations using *DRACO*. As mentioned in the **Shock Transit** section (p. 142), imbalances between beams result in long-wavelength modes on target. Even modes between 2 and 10 are used to simulate the effect of low-order modes using the amplitudes in Fig. 99.3. The

power in odd modes is added in quadrature to the even-mode amplitudes. Figure 99.13 shows the fuel–shell interface amplitudes versus time for the dominant modes in the simulation for the 20- $\mu\text{m}$ -thick shell implosion. The initially unperturbed interface acquires a perturbation shortly after shock breakout around 0.4 ns. When the compression wave returns to the interface, it causes another jump in the perturbation around 0.8 ns. Significant growth is simulated after this time due to the feedthrough of the perturbation from the ablation surface and the convergent Richtmyer–Meshkov instability. Modes 6 and up start oscillating shortly after the end of the acceleration phase as they decouple from the ablation surface. The reflected shock from the center returns to the interface around 1.75 ns, when  $\ell = 4$  changes phase. Rayleigh–Taylor growth occurs shortly after that as the shell continuously decelerates toward stagnation.

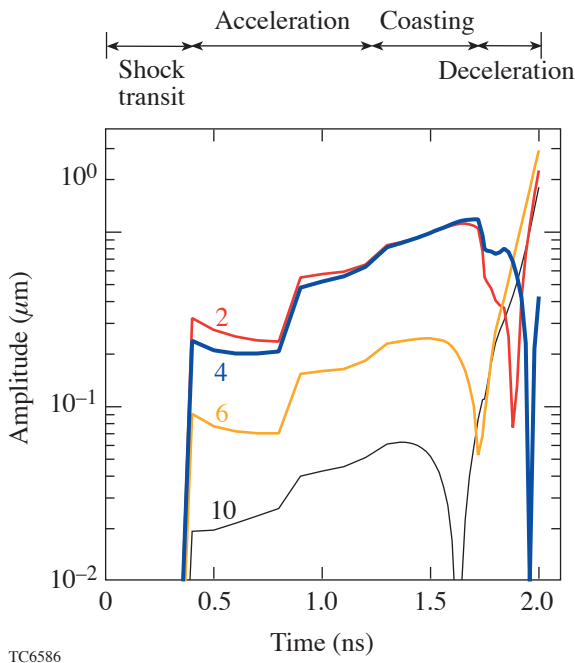


Figure 99.13

Modal amplitudes versus time at the fuel–shell interface for the low-order multimode simulation (due to beam imbalances) of a 20- $\mu\text{m}$ -thick CH shell. The interface becomes perturbed shortly after shock breakout around 0.4 ns. A second jump in the amplitude is modeled at  $\sim 0.8$  ns when the second shock breaks out of the shell. Shorter wavelengths such as modes 6 and 10 decouple during the coasting phase when they change phase. Longer wavelengths (modes 2 and 4) change phase when the shock returns to the interface at  $\sim 1.75$  ns.

The yield is only marginally affected by low-order modes with 2-D simulation, resulting in  $\sim 95\%$  of the 1-D yield for the 20- $\mu\text{m}$ -thick shell and  $\sim 94\%$  of 1-D for the 27- $\mu\text{m}$ -thick shell.

Figure 99.14 shows the density contours at peak neutron production for the 20- $\mu\text{m}$ -thick implosion. The  $\text{D}_2$ –CH interface is marginally distorted. Areal-density variations of  $\sim 23\%$  at peak neutron production (for both shell thicknesses) are simulated.

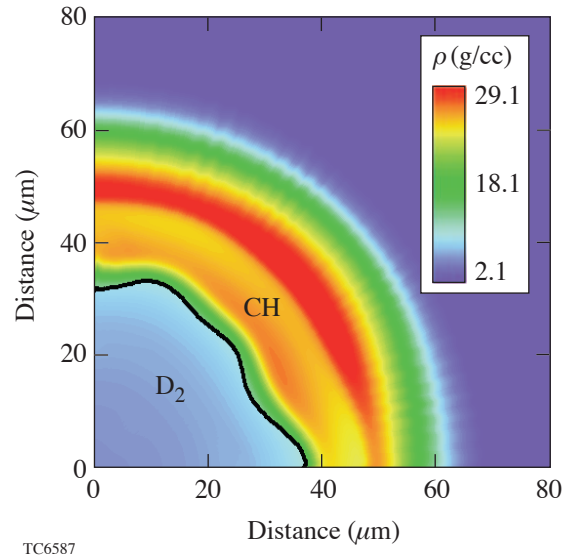


Figure 99.14

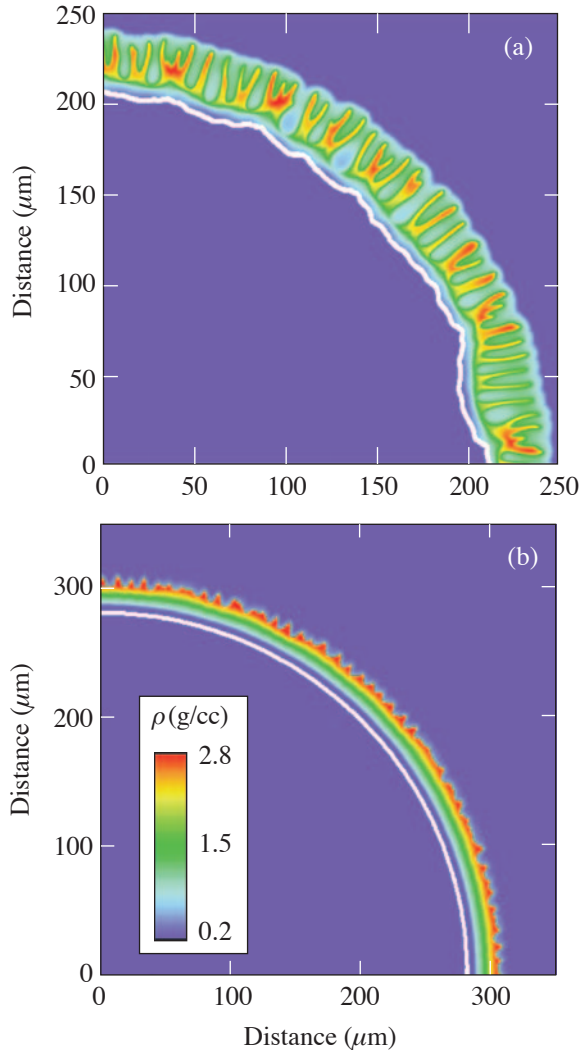
Density contours at peak neutron production from a multimode simulation including only low- $\ell$  modes ( $\ell < 10$ ) for the 20- $\mu\text{m}$ -thick CH implosion. An areal-density variation of 23% is calculated at this time in the implosion. The solid line corresponds to the  $\text{D}_2$ –CH interface.

The marginal effect of low-order modes is consistent with the experimental beam-balancing work described in Ref. 37. In that work, on-target beam balance was changed in a controlled manner; the estimated decrease in the amplitude of these modes was between 30%–50%. While a decrease in areal-density variations was observed, only a marginal difference was observed in absolute neutron yields.

## 2. Effects of Single-Beam Nonuniformity

Single-beam nonuniformity influences intermediate- and short-wavelength seeds on target. As mentioned earlier, modes up to at least 400 are required to realistically model shell stability. A full 2-D simulation including the effects of power imbalance would then require modes between 2 and 400. Resolving mode 400 in such a simulation requires a large number of computational zones—far beyond the scope of this work. We illustrate the effect of laser imprint on shell stability by performing simulations with a smaller set of modes. The simulations include beam-smoothing techniques modeled as

described in the **Acceleration Phase** section (p. 145). Figure 99.15(a) shows a plot of density contours at the end of the acceleration phase from a simulation that includes even modes up to  $\ell = 200$  for the 20- $\mu\text{m}$ -thick CH shell. The shortest wavelength in this simulation is resolved using 14 cells, resulting in a  $200 \times 700$  zone simulation. Since odd modes are not included in the simulation, their power is added in quadrature to the amplitudes of the even modes. The shell indicated by the high-density regions is considerably distorted with portions of the shell at less than solid densities. The peak-to-



TC6588

Figure 99.15  
Density contours at the end of the acceleration phase for (a) a 20- $\mu\text{m}$ -thick CH shell and (b) a 27- $\mu\text{m}$ -thick CH shell from a multimode simulation of laser imprint. The solid lines correspond to the  $\text{D}_2$ -CH interface. Note that the shell (indicated by the higher-density contours) is significantly more distorted for the 20- $\mu\text{m}$  implosion than the 27- $\mu\text{m}$  implosion.

valley variation in the center-of-mass radius is calculated to be 6.6  $\mu\text{m}$  at the end of the acceleration phase, significantly greater than the 1-D shell thickness of  $\sim 5 \mu\text{m}$ . It is expected that shell distortion will increase only when even-shorter wavelengths are included in the calculation. Therefore, short wavelengths play an important role in increasing the adiabat of the shell by introducing additional degrees of freedom for the fluid flow. This will influence the compressibility of the shell and, therefore, neutron yields. In comparison, the 27- $\mu\text{m}$ -thick implosion [Fig. 99.15(b)] has an integral shell at the end of the acceleration phase with a peak-to-valley amplitude of 3.4  $\mu\text{m}$  in the center-of-mass radius compared to a shell thickness of  $\sim 6.8 \mu\text{m}$ . The effect of the still-shorter wavelengths not included in the calculation ( $\ell > 200$ ) can be estimated using a RT postprocessor<sup>31</sup> to the 1-D simulation. This postprocessor indicates that the thicker, 27- $\mu\text{m}$ -thick shell remains integral during the acceleration phase while the stability of the 20- $\mu\text{m}$ -thick shell is severely compromised.

Due to the large number of computational cells in these simulations, it is extremely challenging to reliably simulate these implosions until peak compression. Instead, we assess the effect of the various nonuniformity sources by simulations that include only a few modes but represent reasonably well the shell's stability. The goal of these simulations is to identify the mechanisms that influence neutron yields. More-detailed comparisons with experimental observables will be performed in the future.

### Combined Effects of All Sources of Nonuniformity

Simulations that include a few modes are useful to shed light on which modes influence target performance. The mode ranges are divided into three regions: long wavelengths ( $\ell \leq 10$ ), intermediate wavelengths ( $10 \leq \ell \leq 50$ ), and shorter wavelengths that include all the higher mode numbers. In the **Effects of Beam-to-Beam Imbalances** section (p. 149), it has been pointed out that low-order modes ( $\ell \leq 10$ ) alone have a marginal influence on target performance. We consider simulations involving two modes corresponding to mode numbers 4 and 20 that combine the effect of long and intermediate wavelengths. These simulations and those described later are performed on a  $45^\circ$  wedge. The initial amplitude for each mode is chosen from the amplitudes added in quadrature of a range of mode numbers (from the DPP spectrum for  $\ell = 20$  using modes between 15 and 40 as the mode range and from the initial power balance and surface-roughness data for modes  $2 < \ell < 10$  for mode  $\ell = 4$ ). The neutron-production rate is shown in Fig. 99.16(a) for the 20- $\mu\text{m}$ -thick implosion and Fig. 99.16(b) for the 27- $\mu\text{m}$ -thick implosions. The rate from

the two-mode simulation (dotted line) deviates from the 1-D simulation, and the burn truncates relative to 1-D. This is the case for both thicknesses. The two-mode simulation illustrates the mechanisms for yield reduction through burn truncation. The RT and RM growth at the fuel–shell interface results in the flow of fuel into the colder bubbles, decreasing the yield. This is illustrated in Fig. 99.17, where the fluid velocity vectors

(arrows) in the frame moving radially with the fluid are overlaid on the contour plot of ion temperature at peak neutron production. This result is shown from a single-mode simulation of mode number 20, where this mode has the same initial amplitude as the previous two-mode simulation. Due to heat conduction, the temperature contours are more spherically symmetric than the material interface (solid line). As the vectors indicate, fuel flows into the colder bubbles. This truncates the neutron-production rate. The second mechanism for the truncation of the neutron rate occurs because of the distortion of the high-density shell. The increased surface area enhances heat conduction out of the core, cooling the fuel and decreasing the yield. These mechanisms for the truncation of neutron yield cannot be included in 1-D mix models that have been used previously to model these implosions.<sup>6,8,49</sup> It is also to be noted that the single intermediate-mode simulation has a yield relative to 1-D of 78% (for both thicknesses). The addition of long wavelengths ( $\ell = 4$ ) reduces this value to 55% for the 20- $\mu\text{m}$ -thick shell and 61% for the 27- $\mu\text{m}$ -thick shell. Thus, the combination of the low and intermediate modes has a greater effect on yield than each range of modes alone.

To investigate the role of the shorter wavelengths on yield, we perform a three-mode simulation including mode numbers 4, 20, and 200. In this simulation, modes 4 and 20 have the

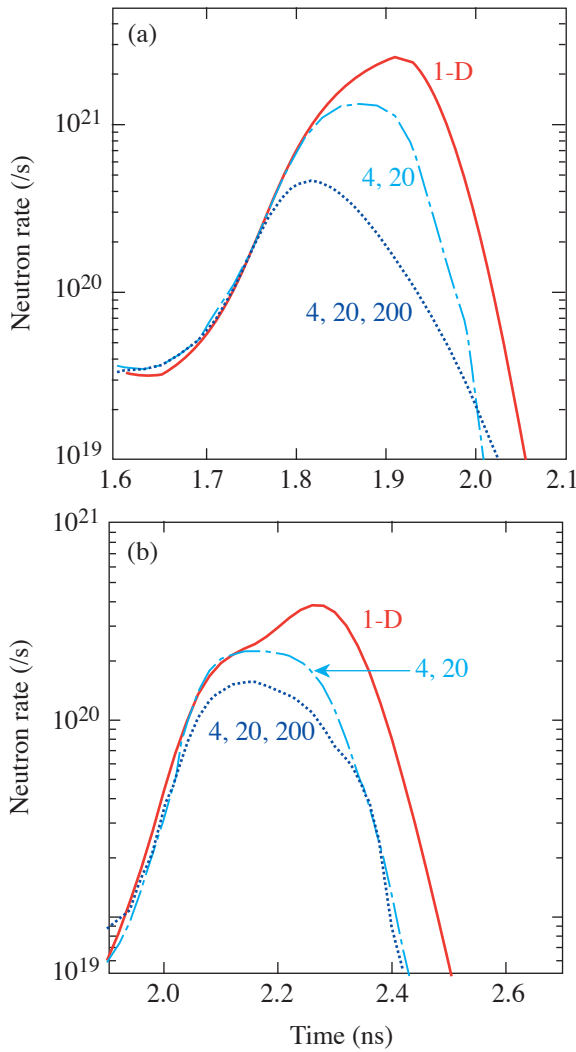


Figure 99.16 Neutron-production rates from the simulation including only low- and intermediate-mode numbers (dashed-dotted line) and the simulation including short wavelengths (dotted line) compared to 1-D (solid line) for (a) the 20- $\mu\text{m}$ -thick CH shell and (b) the 27- $\mu\text{m}$ -thick CH shell. Note that the addition of mode 200 in the simulation including short wavelengths results in a less-steep fall of the neutron production rate for the 20- $\mu\text{m}$  implosion and retains burn truncation for the 27- $\mu\text{m}$  case.

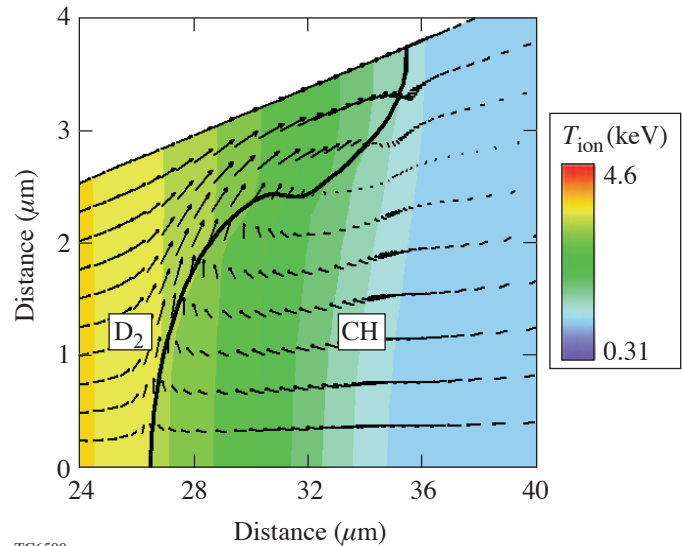


Figure 99.17 Fluid velocity vectors in a frame moving radially with the fluid overlaid on a contour plot of ion temperature at peak neutron production for the 20- $\mu\text{m}$ -thick CH shell. The simulation, from a single-mode perturbation, illustrates one mechanism for burn truncation. As the velocity vectors indicate, fuel flows into the colder bubbles due to RT growth resulting in burn truncation.

same amplitude as the simulation discussed earlier. The amplitude for mode  $\ell = 200$  is chosen by adding in quadrature the power between modes 100 and 300. Contours of mass density for the two shell thicknesses are shown at peak neutron production in Fig. 99.18. The significant shell distortion corresponds to the intermediate mode  $\ell = 20$ . Even though the growth rate at the  $D_2$ -CH interface is highly nonlinear for the short wavelength ( $\ell = 200$ ), the bubble amplitude is, at most,  $1 \mu\text{m}$ . Larger mixing widths ( $\sim 20 \mu\text{m}$ ) have been inferred based on

spherically symmetric 1-D mix models.<sup>6,8</sup> Since 1-D mix models need to account for the increased volume due to long-wavelength distortions, it is very likely that they overestimate the mixing length. An order of magnitude estimate for the mixing length can be obtained as follows: since a hydrodynamic code such as *DRACO* cannot follow materials into the turbulent regime, we consider the amplitude of the short wavelength as a “mix thickness.” The simulated thickness is consistent with expectations from turbulent mixing. The turbulent-mixing layer grows self-similarly with a mixing thickness  $h$ , given by Ref. 50:

$$h = \alpha A_T g t^2, \tag{11}$$

where  $\alpha$  is a dimensionless constant.

As described in the **Deceleration Phase** section (p. 148), bremsstrahlung cooling increases CH density in the hot spot. Consequently, the Atwood number varies continuously during the deceleration phase, reaching a maximum value of 0.5. The increased density, however, does not significantly alter the perturbation growth rate of short wavelengths due to the stabilizing effects of the density-gradient scale length and thermal conduction. Taking  $A_T = 0.18$  for the  $D_2$ -CH interface gives  $\alpha = 0.05$  (Ref. 48), which leads to  $h = 0.9 \mu\text{m}$ . This compares favorably with the amplitude of  $\ell = 200$  inferred from simulation. In previous work, homogenous mixing of  $D_2$  and  $CH$ <sup>6-8,49</sup> has been inferred from experimental observables such as secondary neutron ratios,<sup>6,8</sup> argon spectral lines,<sup>7</sup>  $D^3He$  yields in  $^3He$ -filled CD shells,<sup>6,8</sup> etc. Primary neutron yields have not been used directly to determine the presence of turbulence. The relatively small turbulent mixing layer (compared to the overall deformation of the interface due to intermediate mode numbers) suggests that the experimentally inferred turbulence plays a small role in determining primary neutron yields.

The simulations including  $\ell = 200$  also indicate an interesting trend in neutron production when compared to the simulations including only low and intermediate modes (Fig. 99.16). For both shell thicknesses, the peak in the neutron-production rate deviates earlier. For the  $20\text{-}\mu\text{m}$ -thick shell, however, neutron production does not decrease as steeply as the previous two-mode simulation. For the  $27\text{-}\mu\text{m}$ -thick shell, the neutron-production history is very similar in width to the two-mode simulation. This difference in trends can be explained as follows: The shell is integral for the  $27\text{-}\mu\text{m}$ -thick shell and the density and temperature distribution compare favorably with 1-D [this is shown in Fig. 99.19(b)]. The solid black line is the

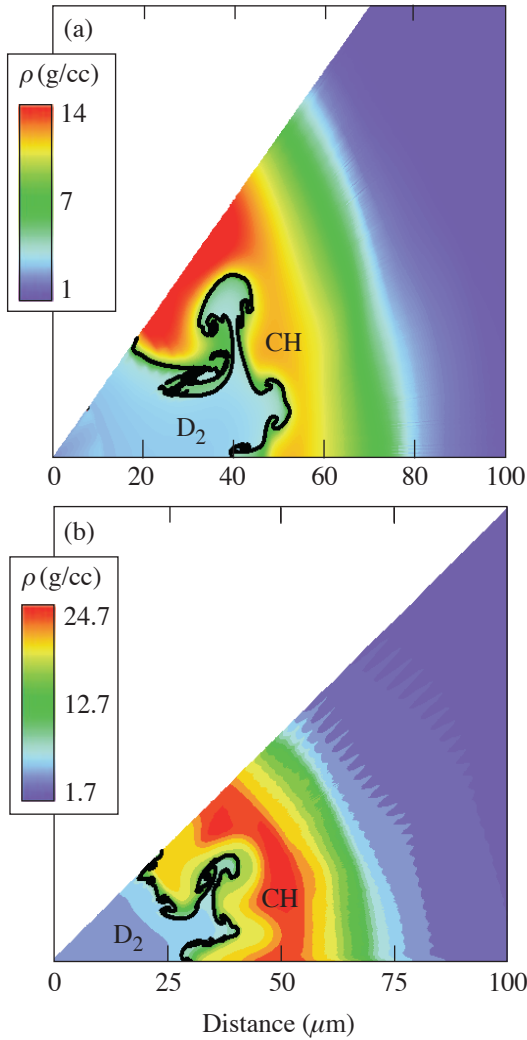
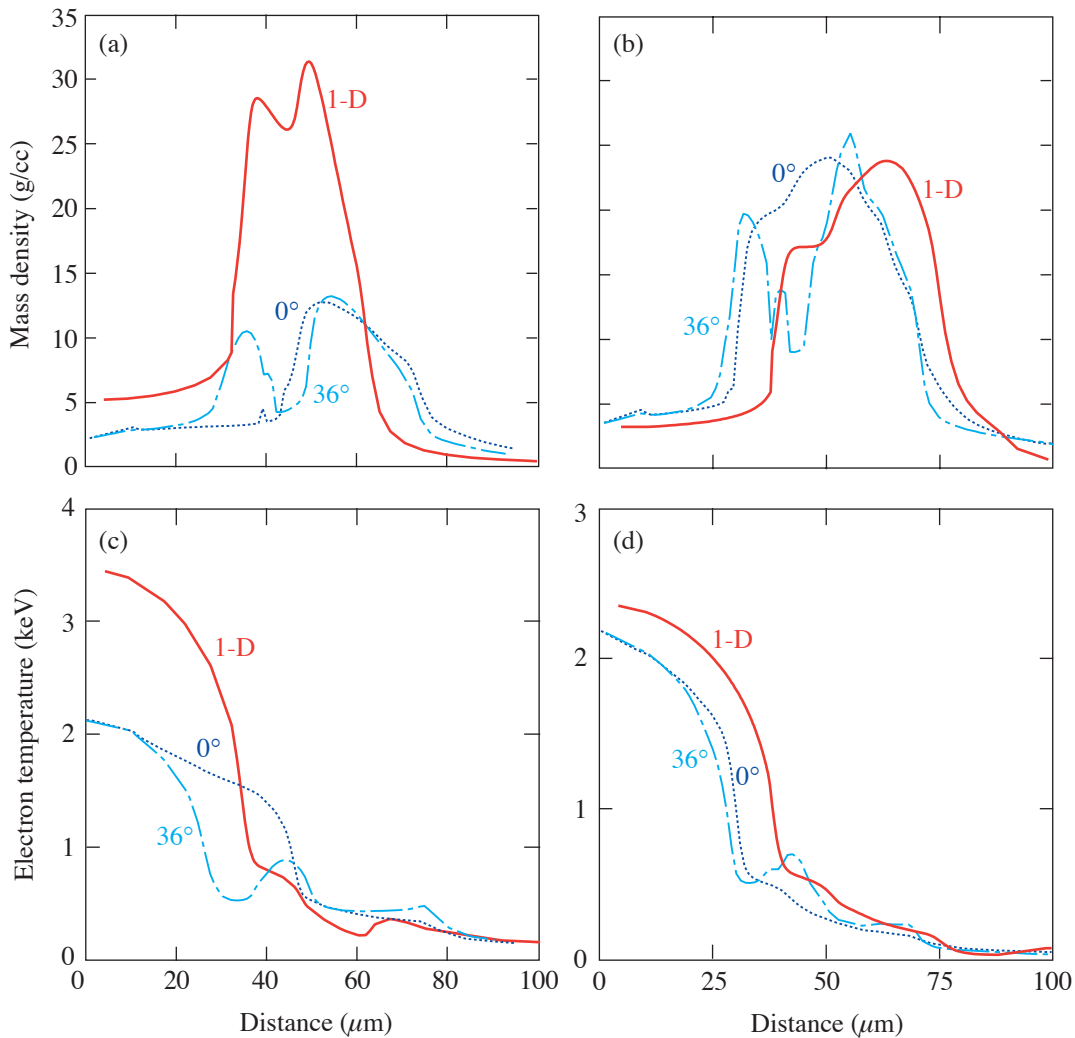


Figure 99.18 Density contours for simulations including short wavelengths at peak neutron production for (a) the  $20\text{-}\mu\text{m}$ -thick CH shell and (b) the  $27\text{-}\mu\text{m}$ -thick CH shell. The solid line is the fuel-shell interface. The short wavelengths ( $\ell \sim 200$ ) have an amplitude of  $\sim 1 \mu\text{m}$ , consistent with estimates of mixing thicknesses from turbulence observations.<sup>48</sup>

1-D result, whereas the other two lines correspond to radial lineouts from the simulations (dashed–dotted at  $36^\circ$  and dotted at  $0^\circ$ ). For the  $20\text{-}\mu\text{m}$ -thick shell, the profiles from the 2-D simulation are significantly different from 1-D [Fig. 99.19(a)]. The peak densities are much lower, and the shell has a wider extent due to the increased adiabat from shell breakup during acceleration. This profile results in delayed stagnation as the shock takes much longer in this case to reach the back of the shell [see the **Deceleration Phase** section (p. 148)]. This delayed shell disassembly results in a persistence of neutron

production compared to the simulation including only low and intermediate modes. Figures 99.19(c) and 99.19(d) show the corresponding radial temperature lineouts from the simulation. The lower temperature in the  $27\text{-}\mu\text{m}$  implosion [Fig. 99.19(d)] is caused by shell distortion and increased heat flow from the core. The  $20\text{-}\mu\text{m}$  implosion [Fig. 99.19(c)], in addition, shows lower temperature caused by the decreased compression. The yields relative to 1-D are 21% for the  $20\text{-}\mu\text{m}$ -thick CH shell compared to 47% for the  $27\text{-}\mu\text{m}$ -thick CH shell. Experimentally, the yields relative to 1-D are



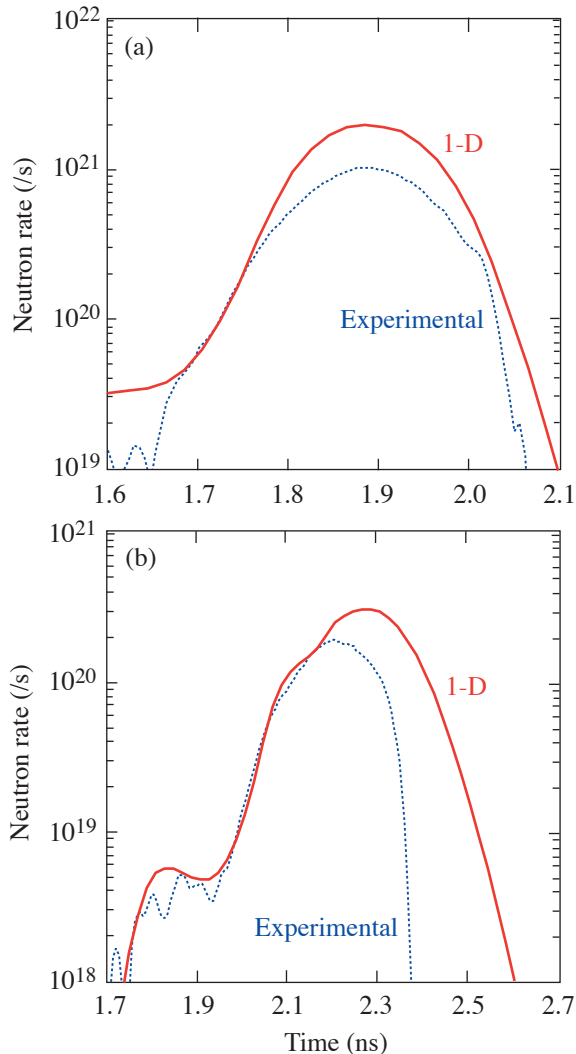
TC6592 &amp; TC6593

Figure 99.19

Radial lineouts of density from the simulation including short wavelengths for (a) the  $20\text{-}\mu\text{m}$ -thick CH shell and (b) the  $27\text{-}\mu\text{m}$ -thick CH shell at two different polar angles [ $0^\circ$  (dotted) and  $36^\circ$  (dashed–dotted)], compared to the 1-D simulation (solid line). Note that the thinner shell has significantly lower densities compared to 1-D. The shell is considerably thicker for the  $20\text{-}\mu\text{m}$  implosion. Radial lineouts of temperature are shown for (c) the  $20\text{-}\mu\text{m}$  implosion and (d) the  $27\text{-}\mu\text{m}$  implosion. All lineouts are at peak neutron production in 1-D. The temperatures in the core are lower than 1-D due to enhanced heat conduction out of the distorted core (both thicknesses) and the overall lower compression in the  $20\text{-}\mu\text{m}$ -thick implosion.

$\sim 40\%$  and  $\sim 45\%$  for the  $20\text{-}\mu\text{m}$  and  $27\text{-}\mu\text{m}$  thicknesses, respectively. Since mode  $\ell = 200$  has a larger effect on the  $20\text{-}\mu\text{m}$  implosion, the smaller yield relative to 1-D in the simulation for the  $20\text{-}\mu\text{m}$  implosion points to an overestimate of the initial amplitude of  $\ell = 200$  in the simulation.

Similar trends in neutron-production rates are observed in experiments. Figure 99.20 shows the neutron-production rates



TC6594

Figure 99.20 Comparison of calculated (1-D) neutron rates (solid line) with experiment (dotted) for (a) the  $20\text{-}\mu\text{m}$ -thick implosion (shot number 30628) and (b) the  $27\text{-}\mu\text{m}$ -thick implosion (shot number 22088). Burn truncation is evident for the  $27\text{-}\mu\text{m}$ -thick implosion. Neutron production rate persists and is almost as wide as 1-D for the  $20\text{-}\mu\text{m}$ -thick implosion.

from experiment (dotted line), and the 1-D simulation (solid line), for the  $20\text{-}\mu\text{m}$ -thick implosion [Fig. 99.18(a)] and the  $27\text{-}\mu\text{m}$ -thick implosion [Fig. 99.18(b)]. Since absolute timing in these experiments was unknown, the 1-D rates are overlaid on the experimental rates by aligning the rise times of the two neutron-rate curves. For the thinner shell, the experimental burnwidth is closer to 1-D, whereas for the thicker, more-stable shell, the burnwidth is truncated compared to 1-D. This trend persists: a still thicker shell ( $33\text{ }\mu\text{m}$ ) shows increased burn truncation, and even thinner shells ( $15\text{ }\mu\text{m}$ ) indicate a widening of the neutron-production history. The 2-D simulation of the  $20\text{-}\mu\text{m}$  implosion shows a slower fall of the neutron-production rate compared to the experimentally observed rate. This is likely due to the larger value for the initial amplitude of the  $\ell = 200$  mode in the simulation compared to that in the experiment.

In summary, the combination of intermediate and low modes significantly influences yields, which manifests itself as burn truncation in the neutron-production rates. The short wavelengths significantly affect shell stability for the thinner shells and can consequently influence stagnation. This in turn widens the burnwidth and also influences yields. For the thicker shells, the burnwidth does not change significantly with the addition of short-wavelength modes. In both cases, the neutron rates deviate earlier from 1-D with the addition of short wavelengths in simulation.

## Conclusions

One-dimensional dynamics of plastic-shell implosions of two different thicknesses irradiated by a smooth laser is discussed. Seeding and evolution of nonuniformities are discussed for the different phases of the implosion. We show that during the acceleration phase, modes up to at least  $\sim 400$  should contribute to shell stability. Multimode simulations using the code *DRACO* indicate that the shell stability in the implosion of a  $20\text{-}\mu\text{m}$ -thick plastic shell is significantly compromised due to Rayleigh–Taylor instability during the acceleration phase, whereas the  $27\text{-}\mu\text{m}$ -thick shell is only marginally distorted. Long-wavelength multimode simulations indicate that imbalances between the laser beams have a small effect on target yields. Intermediate modes appear to influence yields significantly. Short wavelengths result in qualitatively different behavior between the two shell thicknesses: widening the burnwidth for the thinner shell and marginally influencing burnwidth for the thicker shell. This trend in neutron-production rates is also observed in experiment. Future work will include detailed comparisons of charged-particle spectra with experimental observations, an additional analysis to relate

small-scale mix thicknesses to observations of homogenous mixing in experiments, and the comparison of x-ray images of the compressed core with experiments.

#### ACKNOWLEDGMENT

This work was supported by the U.S. Department of Energy Office of Inertial Confinement Fusion under Cooperative Agreement No. DE-FC52-92SF19460, the University of Rochester, and the New York State Energy Research and Development Authority. The support of DOE does not constitute an endorsement by DOE of the views expressed in this article. This work has been supported in part by LLE (subcontract PO412163G) with the University of Wisconsin for the implementation of the PetSc Libraries in *DRACO*.

#### Appendix A: Seeding of the Long-Wavelength Modes due to Drive Asymmetry

The nonuniformities in laser intensity result in asymmetries in drive pressure  $\Delta P$ . To relate the ablation pressure and laser-intensity nonuniformities  $\Delta I$ , we adopt the “cloudy-day” model.<sup>38</sup> Using the scaling  $P \sim I^{2/3}$  yields the following relation:

$$\frac{\Delta P}{P} \approx \frac{2}{3} \frac{\Delta I}{I} e^{-kD_c} \equiv \frac{2}{3} \tilde{I}, \quad (\text{A1})$$

where  $D_c$  is the size of the conduction zone (the distance between the ablation front and critical surface) and  $k$  is the wave number. For the set of experiments described in this article, the conduction zone grows linearly in time,  $D_c = V_c t$  with  $V_c \approx 68 \mu\text{m/ns}$ . Since the laser intensity is spatially modulated, the shocks driven by the peaks in the laser illumination travel faster than the shocks launched at the intensity minimums; therefore, the shock and ablation fronts get distorted. This distortion growth can be estimated for long-wavelength modes using the following simple model: The shock velocity, in the strong-shock limit, is proportional to the square root of the drive pressure  $P$ :

$$U_s \approx \sqrt{\frac{\gamma+1}{2} \frac{P}{\rho_0}}, \quad (\text{A2})$$

where  $\rho_0$  is the initial (undriven) shell density and  $\gamma$  is the ratio of specific heats ( $\gamma = 5/3$  for the monoatomic ideal gas). Modulations in the drive pressure distort the shock front according to

$$\frac{d\eta_s}{dt} = \Delta U_s = \frac{dU_s}{dP} \Delta P_s \approx \frac{2}{\sqrt{5}} c_s \frac{\Delta P}{P}, \quad (\text{A3})$$

where  $c_s$  is the sound speed of the shock-compressed shell,  $\Delta P_s$  is the pressure modulation at the shock, and  $\eta_s$  is the

shock-front modulation. We approximate  $\Delta P$  in the latter equation with the modulation at the ablation front [Eq. (A1)]. Such an approximation is justified only for the long-wavelength modes when the lateral fluid motion can be neglected. The distortion in the ablation front is caused by the perturbations in the post-shock velocity  $U_{ps} = -\rho_0/\rho U_s$ , where  $U_{ps}$  is calculated in the shock frame of reference. Such perturbations are due to (1) modulations in the shock velocity,  $-(\rho_0/\rho)\Delta U_s$ ; (2) modulations  $\Delta\rho$  in the shock-compressed density,  $(\rho_0/\rho)(\Delta\rho/\rho)U_s$ ; and (3) modulations in the position of the shock front. It can be shown that the density modulation right behind the shock is small for strong shocks ( $\Delta\rho/\rho \sim M_s^{-2} \Delta P/P$ , where  $M_s$  is the shock Mach number) and can be neglected. The resulting modulation in the post-shock velocity takes the form

$$\Delta U_{ps} = (\rho_0/\rho - 1)\Delta U_s = \frac{3}{4}\Delta U_s. \quad (\text{A4})$$

Since ablative stabilization and lateral flow can be neglected for the long-wavelength modes,  $d\eta_a/dt = \Delta U_{ps}$ . Integrating the latter equation gives the ablation-front modulation  $\eta_a$ :

$$\eta_a(t) = \frac{1}{\sqrt{5}} \int_0^t dt' \tilde{I}(t') c_s(t'), \quad \eta_s = \frac{4}{3} \eta_a. \quad (\text{A5})$$

It is also important to determine the modulation in the CH–gas interface  $\eta_{\text{int}}$  at the beginning of the acceleration phase. The modulation at the interface is seeded by the perturbed shock. As soon as the shock breaks out of the shell, the rear surface starts to expand with the velocity  $3c_s$  (Ref. 51) with respect to the shock-compressed material. Therefore, the amplitude of the CH–gas interface takes the value  $\eta_{\text{int}} = 3c_s \delta t$ , where  $\delta t = \eta_s/U_s$  is the shock transit time across the modulation amplitude. Using the strong shock limit, one obtains  $\eta_{\text{int}} = 3\sqrt{5}\eta_s/4$ . Taking into account the relation between  $\eta_s$  and  $\eta_a$  yields  $\eta_{\text{int}} = \sqrt{5}\eta_a$ . As shown in Ref. 52, the gas–CH interface is unstable during the rarefaction-wave (RW) propagation through the shell. Since such a growth is linear in time and proportional to the modulation wave number, there is very little change in the amplitude of the fuel–pusher interface between the shock breakout and the beginning of the acceleration phase. To determine the mode amplitudes at the beginning of the acceleration phase, we integrate Eq. (A5) using the laser nonuniformity profiles shown in Fig. 99.3. The spectrum thus obtained is plotted in Fig. 99.4 and compared against the results of the full 2-D power-balance simulation. Observe that the simple model reproduces the results of simulations very well. To calculate the initial conditions for the RT growth, in addition to the initial

amplitude, we must calculate the perturbed front velocity  $\eta'_a$ . This velocity has two components: the first is given by Eqs. (A3) and (A4), and the second is due to the rippled RW breakout at the ablation front. Indeed, when the first shock reaches the rear surface, the RW is launched toward the ablation front. The RW travels with the local sound speed  $c_s$ ; therefore, if the shock amplitude is  $\eta_s$ , the rarefaction amplitude then becomes  $\eta_{RW} = c_s(\eta_s/U_s) = \sqrt{5}\eta_s/4$ . The phase of the modulation in the rarefaction head is opposite to the phases of the rear-surface and ablation-front perturbations. Upon reaching the ablation front, the leading edge of the RW establishes the pressure gradient, accelerating the front. Since the peaks of the RW break out at the ablation front prior to the valleys, the ablation-front ripple gains an additional velocity perturbation  $\delta v = g\delta t$ , where  $g$  is the acceleration and  $\delta t = \eta_{RW}/c_s = \sqrt{5}/3(\eta_a/c_s)$ . Combining the two contributions, the initial ripple velocity takes the form

$$\frac{d\eta_a}{dt}(t_0) = \tilde{I}(t_0) \frac{c_s}{\sqrt{5}} + \frac{\sqrt{5}g}{3c_s} \eta_a(t_0), \quad (\text{A6})$$

where  $t_0$  is the time at the beginning of acceleration phase. Equations (A5) and (A6) show that the ablation-front amplitude changes slope at  $t = t_0$ . Substituting  $g = c_s^2/(\gamma\Delta_{sh})$  into Eq. (A6) and also approximating  $\eta_a(t_0) \sim \langle \tilde{I} \rangle_{sh} (c_s/U_{sh}) 4\Delta_{sh}$ , we can rewrite Eq. (A6) as

$$\eta'_a(t_0) \sim \tilde{I}(t_0) \frac{c_s}{\sqrt{5}} + \langle \tilde{I} \rangle_{sh} \frac{c_s}{\sqrt{5}}. \quad (\text{A7})$$

The second term on the right-hand side of Eq. (A7) is proportional to the laser nonuniformity averaged over the shock transit time,  $\langle \tilde{I} \rangle_{sh}$ . Taking into account that beam mistiming significantly increases  $\tilde{I}$  at the beginning of the pulse (during the pulse rise),  $\langle \tilde{I} \rangle_{sh}$  becomes much larger than  $\tilde{I}(t_0)$  (in most cases by a factor of 5). This conclusion is valid for a large variety of target designs, including the ignition design, since the laser reaches its peak intensity prior to the acceleration phase. One must keep in mind, however, that Eq. (A6) assumes sharp interfaces of the CH–gas boundary and the ablation front. In reality the radiation preheat relaxes the density at the CH–gas interface prior to the first shock breakout. In addition, the ablation front has a finite thickness. These effects cause deviations of the initial condition from simple estimates [Eqs. (A5) and (A7)]. Comparison with the results of 2-D simulations, however, shows that finite interface thickness effects do not significantly modify the perturbation amplitudes (Fig. 99.4).

## Appendix B: Growth of Long-Wavelength Modes During the Acceleration Phase

The equation describing the perturbation growth for the long-wavelength modes (ablation effects are neglected) during the acceleration phase can be written as<sup>32</sup>

$$\frac{d}{dt} \left( \frac{1}{\rho r} \frac{d}{dt} \rho r^2 \eta \right) - \ell g \eta = \ell \frac{\Delta P}{\rho} = \ell \frac{2}{3} \frac{\delta I}{I} \left( \frac{r}{r_c} \right)^\ell g \Delta_{sh}, \quad (\text{B1})$$

where  $\Delta P$  is the drive-pressure nonuniformity,  $r$  is the shell radius,  $g$  is the shell acceleration,  $\rho$  is the shell density,  $\Delta_{sh}$  is the shell thickness,  $r_c$  is the position of the average laser-deposition surface, and  $\eta$  is the ablation-front modulation amplitude. The factor  $(r/r_c)^\ell$  is due to the cloudy-day effect. Equation (B1) is subject to the initial conditions (A5) and (A6). The shell thickness is  $\Delta_{sh} = 5 \mu\text{m}$  for the 20- $\mu\text{m}$  shell and  $\Delta_{sh} = 6.8 \mu\text{m}$  for the 27- $\mu\text{m}$  shell. During this phase of the implosion, the shell density remains approximately constant, so we can cancel  $\rho$  in Eq. (B1). For simplicity we assume constant shell acceleration  $r = r_0 - gt^2/2$ . To compare a relative importance of the RT growth versus the secular growth during the shell acceleration, we compare  $\ell g \eta$  with the right-hand side of Eq. (B1). The lower limit of this term is

$$\min(\ell g \eta) = \ell g \eta(t_0) \approx \ell g \langle \tilde{I} \rangle_{sh} \frac{\Delta_0}{\sqrt{5}} \frac{c_s}{U_{sh}} = \ell g \Delta_{sh} \langle \tilde{I} \rangle_{sh}, \quad (\text{B2})$$

where  $\Delta_{sh}$  is the in-flight shell thickness (which is approximately four times smaller than the initial thickness  $\Delta_0$ ) and  $\langle \tilde{I} \rangle_{sh}$  is the intensity modulation averaged over the shock-propagation time. Comparing the latter expression with the right-hand side of Eq. (B1), we observe that  $\Delta P/\rho \ll g\eta$  during the acceleration phase. The latter inequality is satisfied for very long wavelengths ( $\ell < 10$ ) because  $\langle \tilde{I} \rangle_{sh} I_{sh} \gg \tilde{I}(t_0)$  due to beam mistiming early in the pulse. Shorter wavelengths ( $\ell > 10$ ), on the other hand, experience a large attenuation due to thermal smoothing in the conduction zone; therefore, the right-hand side of Eq. (B1) is also small for such mode. Thus, we can conclude that the secular growth during the acceleration phase is much smaller than the RT amplification of the initial amplitude and velocity of the ablation-front modulation. This growth can be estimated using the WKB solution of the homogeneous part of Eq. (B1) with the following initial conditions:

$$\eta_0 = \langle \tilde{I} \rangle_{sh} \Delta_{sh}, \quad \eta'_0 = \frac{c_s}{\sqrt{5}} \left[ \tilde{I}(t_0) + \langle \tilde{I} \rangle_{sh} \right]. \quad (\text{B3})$$

Using results of Ref. 31, the solution takes the form

$$\eta_a = C_r^{5/4} \left[ \eta_0 \cosh \Psi + \eta'_0 \sqrt{\frac{r_0}{(\ell+2)g}} \sinh \Psi \right], \quad (\text{B4})$$

where  $\Psi = \sqrt{2(\ell+2)} \arcsin \sqrt{1-C_r^{-1}}$  and  $C_r$  is the convergence ratio during the acceleration phase. During the acceleration phase, the convergence ratio of the 20- $\mu\text{m}$  shell and the 27- $\mu\text{m}$  shell is  $C_r = r_0/r \approx 1.7$  and  $C_r \approx 1.4$ , respectively, where  $r_0 = 430 \mu\text{m}$  is the ablation-front radius at the beginning of the shell acceleration. The dominant role of the RT growth over the secular growth is confirmed by the results of *DRACO* simulation. Figure 99.8 shows a plot of the perturbation amplitude with full power imbalance (dashed-dotted line) and with the power imbalance turned off (solid line) during the acceleration phase.

## REFERENCES

1. J. Nuckolls *et al.*, *Nature* **239**, 139 (1972).
2. C. P. Verdon, *Bull. Am. Phys. Soc.* **38**, 2010 (1993).
3. M. D. Campbell and W. J. Hogan, *Plasma Phys. Control. Fusion* **41**, B39 (1999).
4. T. R. Boehly, D. L. Brown, R. S. Craxton, R. L. Keck, J. P. Knauer, J. H. Kelly, T. J. Kessler, S. A. Kumpan, S. J. Loucks, S. A. Letzring, F. J. Marshall, R. L. McCrory, S. F. B. Morse, W. Seka, J. M. Soares, and C. P. Verdon, *Opt. Commun.* **133**, 495 (1997).
5. D. D. Meyerhofer, J. A. Delettrez, R. Epstein, V. Yu. Glebov, V. N. Goncharov, R. L. Keck, R. L. McCrory, P. W. McKenty, F. J. Marshall, P. B. Radha, S. P. Regan, S. Roberts, W. Seka, S. Skupsky, V. A. Smalyuk, C. Sorce, C. Stoeckl, J. M. Soares, R. P. J. Town, B. Yaakobi, J. D. Zuegel, J. Frenje, C. K. Li, R. D. Petrasso, D. G. Hicks, F. H. Séguin, K. Fletcher, S. Padalino, M. R. Freeman, N. Izumi, R. Lerche, T. W. Phillips, and T. C. Sangster, *Phys. Plasmas* **8**, 2251 (2001).
6. P. B. Radha, J. Delettrez, R. Epstein, V. Yu. Glebov, R. Keck, R. L. McCrory, P. McKenty, D. D. Meyerhofer, F. Marshall, S. P. Regan, S. Roberts, T. C. Sangster, W. Seka, S. Skupsky, V. Smalyuk, C. Sorce, C. Stoeckl, J. Soares, R. P. J. Town, B. Yaakobi, J. Frenje, C. K. Li, R. Petrasso, F. Séguin, K. Fletcher, S. Padalino, C. Freeman, N. Izumi, R. Lerche, and T. W. Phillips, *Phys. Plasmas* **9**, 2208 (2002).
7. S. P. Regan, J. A. Delettrez, F. J. Marshall, J. M. Soares, V. A. Smalyuk, B. Yaakobi, V. Yu. Glebov, P. A. Jaanimagi, D. D. Meyerhofer, P. B. Radha, W. Seka, S. Skupsky, C. Stoeckl, R. P. J. Town, D. A. Haynes, Jr., I. E. Golovkin, C. F. Hooper, Jr., J. A. Frenje, C. K. Li, R. D. Petrasso, and F. H. Séguin, *Phys. Rev. Lett.* **89**, 085003 (2002).
8. C. K. Li, D. G. Hicks, F. H. Séguin, J. Frenje, R. D. Petrasso, J. M. Soares, P. B. Radha, V. Yu. Glebov, C. Stoeckl, J. P. Knauer, F. J. Marshall, D. D. Meyerhofer, S. Skupsky, S. Roberts, C. Sorce, T. C. Sangster, T. W. Phillips, and M. D. Cable, *Rev. Sci. Instrum.* **72**, 864 (2001).
9. D. Keller, T. J. B. Collins, J. A. Delettrez, P. W. McKenty, P. B. Radha, B. Whitney, and G. A. Moses, *Bull. Am. Phys. Soc.* **44**, 37 (1999).
10. Lord Rayleigh, *Proc. London Math Soc.* **XIV**, 170 (1883); G. Taylor, *Proc. R. Soc. London Ser. A* **201**, 192 (1950).
11. S. E. Bodner, *Phys. Rev. Lett.* **33**, 761 (1974).
12. H. Takabe *et al.*, *Phys. Fluids* **28**, 3676 (1985).
13. R. Betti, V. N. Goncharov, R. L. McCrory, P. Sorotokin, and C. P. Verdon, *Phys. Plasmas* **3**, 2122 (1996).
14. G. I. Bell, Los Alamos National Laboratory, Los Alamos, NM, Report LA-1321 (1951).
15. M. S. Plesset, *J. Appl. Phys.* **25**, 96 (1954); D. L. Book and S. E. Bodner, *Phys. Fluids* **30**, 367 (1987); Laboratory for Laser Energetics LLE Review **94**, 81, NTIS document No. DOE/SF/19460-485 (2003). Copies of the last item may be obtained from the National Technical Information Service, Springfield, VA 22161.
16. M. C. Richardson, G. G. Gregory, R. L. Keck, S. A. Letzring, R. S. Marjoribanks, F. J. Marshall, G. Pien, J. S. Wark, B. Yaakobi, P. D. Goldstone, A. Hauer, G. S. Stradling, F. Ameduri, B. L. Henke, and P. Jaanimagi, in *Laser Interaction and Related Plasma Phenomena*, edited by H. Hora and G. H. Miley (Plenum Press, New York, 1986), Vol. 7, pp. 179–211.
17. A. A. Amsden, H. M. Ruppel, and C. W. Hirt, Los Alamos National Laboratory, Los Alamos, NM, Report LA-8095 (1980).
18. M. L. Wilkins, *J. Comput. Phys.* **36**, 281 (1980).
19. G. Maenchen and S. Sack, in *Methods in Computational Physics*, edited by B. Alder, S. Fernbach, and M. Rotenberg, *Fundamental Methods in Hydrodynamics* (Academic Press, New York, 1964), Vol. 3, pp. 181–210.
20. A. M. Winslow, *J. Comput. Phys.* **2**, 149 (1967); S. Atzeni and A. Guerrieri, *Laser Part. Beams* **9**, 443 (1991); J. U. Brackbill and J. S. Saltzman, *J. Comput. Phys.* **46**, 342 (1982).
21. B. van Leer, *J. Comput. Phys.* **23**, 276 (1977).
22. D. L. Youngs, in *Numerical Methods for Fluid Dynamics*, edited by K. W. Morton and M. J. Baines (Academic Press, London, 1982), pp. 273–285.
23. D. J. Benson, *Comput. Methods Appl. Mech. Eng. (Netherlands)* **99**, 235 (1992).
24. S. P. Lyon and J. D. Johnson, Los Alamos National Laboratory, Los Alamos, NM, Report LA-UR-92-3407 (1992).
25. A. R. Bell, Rutherford Appleton Laboratory, Chilton, Didcot, Oxon, England, Report RL-80-091 (1980).
26. R. M. More, K. H. Warren, D. A. Young, and G. B. Zimmerman, *Phys. Fluids* **31**, 3059 (1988).
27. W. F. Huebner *et al.*, Los Alamos National Laboratory, Los Alamos, NM, Report LA-6760-M (1977).

28. S. Balay *et al.*, in *Modern Software Tools for Scientific Computing*, edited by E. Arge, A. M. Bruaset, and H. P. Langtangen (Birkhäuser, Boston, 1997), Chap. 8, pp. 163–202.
29. MPI Version 1.2 Standard for IRIX—A Communication Language for Parallel Processing (2001).
30. L. M. Hively, *Nucl. Fusion* **17**, 873 (1977).
31. R. L. McCrory and C. P. Verdon, in *Inertial Confinement Fusion*, edited by A. Caruso and E. Sindoni (Editrice Compositori, Bologna, Italy, 1989), pp. 83–124.
32. V. N. Goncharov, P. McKenty, S. Skupsky, R. Betti, R. L. McCrory, and C. Cherfils-Clérouin, *Phys. Plasmas* **7**, 5118 (2000).
33. S. Skupsky, R. W. Short, T. Kessler, R. S. Craxton, S. Letzring, and J. M. Soures, *J. Appl. Phys.* **66**, 3456 (1989).
34. T. R. Boehly, V. A. Smalyuk, D. D. Meyerhofer, J. P. Knauer, D. K. Bradley, R. S. Craxton, M. J. Guardalben, S. Skupsky, and T. J. Kessler, *J. Appl. Phys.* **85**, 3444 (1999).
35. R. D. Richtmyer, *Commun. Pure. Appl. Math.* **XIII**, 297 (1960); V. A. Andronov *et al.*, *Sov. Phys.-JETP* **44**, 424 (1976).
36. V. N. Goncharov, *Phys. Rev. Lett.* **82**, 2091 (1999).
37. F. J. Marshall, J. A. Delettrez, R. Epstein, R. Forties, R. L. Keck, J. H. Kelly, P. W. McKenty, S. P. Regan, and L. J. Waxer, *Phys. Plasmas* **11**, 251 (2004).
38. S. E. Bodner, *J. Fusion Energy* **1**, 221 (1981).
39. V. N. Goncharov, S. Skupsky, T. R. Boehly, J. P. Knauer, P. McKenty, V. A. Smalyuk, R. P. J. Town, O. V. Gotchev, R. Betti, and D. D. Meyerhofer, *Phys. Plasmas* **7**, 2062 (2000).
40. C. B. Burckhardt, *Appl. Opt.* **9**, 695 (1970).
41. Y. Kato *et al.*, *Phys. Rev. Lett.* **53**, 1057 (1984).
42. Laboratory for Laser Energetics LLE Review **65**, 1, NTIS document No. DOE/SF/19460-117 (1995). Copies may be obtained from the National Technical Information Service, Springfield, VA 22161.
43. R. Epstein, *J. Appl. Phys.* **82**, 2123 (1997).
44. S. P. Regan, J. A. Marozas, J. H. Kelly, T. R. Boehly, W. R. Donaldson, P. A. Jaanimagi, R. L. Keck, T. J. Kessler, D. D. Meyerhofer, W. Seka, S. Skupsky, and V. A. Smalyuk, *J. Opt. Soc. Am. B* **17**, 1483 (2000).
45. R. C. Cook, R. L. McEachern, and R. B. Stephens, *Fusion Technol.* **35**, 224 (1999).
46. R. Betti, V. N. Goncharov, R. L. McCrory, and C. P. Verdon, *Phys. Plasmas* **5**, 1446 (1998).
47. J. P. Knauer, R. Betti, D. K. Bradley, T. R. Boehly, T. J. B. Collins, V. N. Goncharov, P. W. McKenty, D. D. Meyerhofer, V. A. Smalyuk, C. P. Verdon, S. G. Glendinning, D. H. Kalantar, and R. G. Watt, *Phys. Plasmas* **7**, 338 (2000).
48. R. Betti, K. Anderson, V. N. Goncharov, R. L. McCrory, D. D. Meyerhofer, S. Skupsky, and R. P. J. Town, *Phys. Plasmas* **9**, 2277 (2002).
49. D. C. Wilson, C. W. Cranfill, C. Christensen, R. A. Forster, R. R. Peterson, H. M. Hoffman, G. D. Pollak, C. K. Li, F. H. Séguin, J. A. Frenje, R. D. Petrasso, P. W. McKenty, F. J. Marshall, V. Yu. Glebov, C. Stoeckl, G. J. Schmid, N. Izumi, and P. Amendt, *Phys. Plasmas* **11**, 2723 (2004).
50. G. Dimonte, *Phys. Plasmas* **6**, 2009 (1999).
51. L. D. Landau and E. M. Lifshitz, *Fluid Mechanics*, 2nd ed., Course of Theoretical Physics, Vol. 6 (Butterworth-Heinemann, Newton, MA, 1987), p. 36.
52. J. G. Wouchuk and R. Carretero, *Phys. Plasmas* **10**, 4237 (2003).

